# Flow Separation Control over a Rounded Ramp with Spanwise Alternating Wall Actuation

Weidan Ni (倪玮丹)[1,2], Lipeng Lu (陆利蓬)[1,3], Jian Fang (方剑)[2], Charles Moulinec[2], David R Emerson[2] and Yufeng Yao (姚宇峰)[4]

[1] *National Key Laboratory of Science and Technology on Aero-Engine Aero-Thermodynamics, School of Energy and Power Engineering, Beihang University, Beijing, 100191, China*

[2] *Scientific Computing Department, Science & Technology Facilities Council (STFC), Daresbury Laboratory, Warrington, WA4 4AD, UK*

[3] Collaborative Innovation Center of Advanced Aero-Engine, Beijing 100191, China

[4] *Faculty of Environment and Technology, Department of Engineering Design and Mathematics, University of the West of England, Bristol, BS16 1QY, UK*

**Abstract** An implicit large-eddy simulation is carried out to study turbulent boundary-layer separation from a backward-facing rounded ramp with active wall actuation control. This method, called spanwise alternating distributed strips control, is imposed onto the flat plate surface upstream of a rounded ramp by alternatively applying out-of-phase control and in-phase control to the wall-normal velocity component in the spanwise direction. As a result, the local turbulence intensity is alternatively suppressed and enhanced, leading to the creation of vertical shear-layers, which is responsible for the presence of large-scale streamwise vortices. These vortices exert a predominant influence on the suppression of the flow separation. The interaction between the large-scale vortices and the downstream recirculation zone and free shear-layer is studied by examining flow statistics. It is found that in comparison with the non-controlled case the flow separation is delayed, the reattachment point is shifted upstream, and the length of the mean recirculation zone is reduced up to 8.49%. The optimal control case is achieved with narrow in-phase control strips. An in-depth analysis shows that the delay of the flow separation is attributed to the activation of the near-wall turbulence by the in-phase control strips and the improvement of the reattachment location is mainly due to the large-scale streamwise vortices, which enhance the momentum transport between the main flow and separated region.

**Keywords** Implicit Large-eddy Simulation (ILES), Backward-Facing Rounded Ramp, Spanwise Alternating Distributed Strips (SADS) Control, Turbulent Secondary Flow, Flow Separation and Reattachment

## I. INTRODUCTION

Flow control can involve passive or active devices that are able to induce favourable flow characteristics. As noted by Gad-el-Hak [1], modern flow control was introduced by Prandtl [2] using boundary-layer theory with a discussion of experiments where the boundary layer was controlled. Historically, it is clear that boundary-layer control is one of the oldest and most critical aspects of existing flow control methods [3]. In general, flow separation is considered to have negative effects, including an increase in pressure drag, flow blockage, loss of lift, instability, and stall and surge phenomena. Leschziner *et al.* [4] categorised drag control strategies into three groups: the delay of transition, the reduction of near-wall turbulence and the

suppression of separation, in which the latter aims to reduce the pressure drag by suppressing flow separation mainly via momentum transport enhancement. Passive vortex generators (VGs), comprised of arrays of ribs and grooves aligned in the streamwise direction with the order of the local boundary-layer thickness, have been used to control flow separation since Taylor [5] first introduced this control strategy in the late 1940s. The generated large-scale streamwise vortices (LSSVs) by VGs, which can enhance the momentum transport in the boundary layer, are believed to be crucial. Lin [6] showed that low-profile VGs, defined as those with a device height between 10% and 50% of the boundary-layer thickness, can produce streamwise vortices just strong enough to overcome separation without unnecessarily persisting within the boundary layer once the flow control objective is achieved. While this concept works well, VGs still face certain technical difficulties in practical applications such as design integration and manufacturing because of local shape change.

In addition to vortex generators, it has been found that some small-scale passive control strategies, such as alternatively distributed riblets or wall roughness imposed within a turbulent boundary layer, could also induce LSSVs. The first evidence appeared in 2002 when Koeltzsch *et al.* [7] applied convergent and divergent riblets to the inside wall of a turbulent pipe-flow. This study primarily focused on providing a hydrodynamic explanation for the converging texture found on the skin surrounding the sensory receptors of fast swimming sharks. Through tiny surface modifications at the pipe wall, a herringbone riblet arrangement was able to impose large-scale modes onto the outer region of the pipe flow. Nugroho *et al.* [8] extended this research and found that large-scale spanwise periodicity could be induced in a boundary layer by applying a converging-diverging riblet-type surface roughness in a zero-pressure-gradient turbulent boundary layer. Further analysis of the pre-multiplied energy spectra suggested surface roughness radically modifies the largest scale energetic structures. The characteristics of a turbulent boundary layer overlying a complex roughness topography were experimentally explored by Mejia-Alvarez *et al.* [9,10]. A lateral exchange of low- and high-momentum pathways (LMP/HMP, respectively) was observed. Mejia-Alvarez *et al.* [10] suggested that the large-scale LMP/HMP are different from the instantaneous low- and high-momentum regions [11-15]. They could further provide preferential pathways for the instantaneous large-scale motions. The same topography was then studied by Barros *et al.* [16] using stereo particle image velocimetry measurements in the wall-normal-spanwise plane. The spanwise regions between LMPs and HMPs are occupied by swirling motions, suggesting the generation and sustainment of turbulent secondary flows due to the spanwise heterogeneity of the complex roughness under consideration. Turbulent wall-bounded flows over transverse roughness transitions were studied by Willingham *et al.* [17] by using large-eddy simulation (LES). The results showed that LMPs are spatially stationary and flanked by $\delta$-scale (local turbulent boundary-layer thickness) counter-rotating vortices which serve to pump fluid vertically from the wall, ultimately leading to a spanwise variation in the boundary-layer depth. Motivated by the LES work of Willingham *et al.* [17], Bai *et al.*

[18] carried out an experimental investigation on the modifications of turbulence over a wall with spanwise-varying roughness using particle image velocimetry and hotwire anemometry. Conditional average analyses revealed that the observed time-invariant flow structures result from the time-averaged process of instantaneous turbulent events that occur frequently in some scenario. Kevin *et al*. [19] also suggested that the mean secondary flows arise from the averaged process of relatively strong turbulent events that occur preferentially in both time and space. Hinze *et al.* [20,21] analysed secondary motions based on turbulent production and dissipation by applying the usual boundary-layer approximations to the balance equations for turbulence kinetic energy (TKE). They suggested that when the production is greater than the dissipation in a localised region, the turbulence-poor fluid is transported into this region by the generated secondary flow, and in the meantime, the turbulence-rich fluid is flowing out of the region and vice versa.

Parametric investigations of the characteristics of large-scale vortices induced by spanwise inhomogeneity have also been carried out. Nugroho *et al.* [8] suggested that increasing the converging-diverging angle or the viscous-scaled height of riblets resulted in stronger spanwise perturbations. Increasing the fetch seems to cause the perturbations to grow further from the surface, while the overall strength of the induced low- and high-speed regions remains relatively unaltered. Willingham *et al.* [17] found varying the width of the high-roughness strips ($L_s$) had a strong impact on the secondary flow pattern whereas the variations in the ratio of the high roughness length to the low roughness length ($\lambda$) imposed a mild effect. The effect of the strip width on the secondary flow topology was investigated by Stroh *et al.* [22], based on results from a turbulent channel flow with spanwise alternating distributed no-slip and free-slip regions. Using direct numerical simulation (DNS), they found that the width of the free-slip area (note that the effect of free-slip area on the flow field is similar with the low-roughness regions for the flows over rough walls) might be a relevant scaling parameter for the secondary flow topology while the influence of the no-slip spacing is weaker, which is opposite to the conclusion drawn by Willingham *et al.* [17]. Recently, Hwang *et al.* [23] systematically studied the two parameters of the pitch ($P$) and width ($S$) for roughness elements in turbulent boundary layer over longitudinal surface roughness using DNS. Their analysis showed that the size of the secondary flow is mostly determined by the value of $P-S$, *i.e.*, the valley width. This is consistent with the results obtained by Stroh *et al.* [22] that the width of the free-slip region in wall units appears to be an important parameter for the vortex formation. Vanderwel *et al.* [24] concluded that the large-scale secondary flows are accentuated when the adjacent spacing of the roughness elements is roughly proportional to the boundary-layer thickness. Cases with coarser spacings also generate $\delta$-scale secondary flows with tertiary flows located at the centres of the valleys between the elevated roughness strips. Yang *et al.* [25] assessed how the spacing between the adjacent high roughness rows, $s_y$, affects the turbulence structure in channel flows at high Reynolds number. The surface type depends on the value of $s_y/H$, where $H$ is the half-height of the channel. Chung *et al.* [26] analysed the DNS data

in a turbulent channel flow controlled by alternately imposed patches of high and low wall shear stress in the lateral direction on the lower wall of the channel. The effect of the lateral spacing, *s*, of the uniform-stress patches (for both high and low wall shear stress) on the similarity and structure of turbulent inertial motion was investigated. They found that the global outer-layer similarity is maintained when *s* is less than around $0.39H$ or greater than about $6.28H$, where $H$ is the half-height of the channel. The effect of the Reynolds number on the flow field was also studied by Stroh *et al.* [22]. They suggested that flows at $Re_\tau$ = 120 and 360 reveal a very similar flow topology transition to the one at $Re_\tau$ = 180 with the spanwise wavelength of the no-slip and free-slip strips increasing, implying Reynolds number independence of the proposed control method in a turbulent channel flow.

Mejia-Alvarez *et al.* [9,10], Willingham *et al.* [17] and Anderson *et al.* [27] suggested that the transverse variation of the surface drag induced a vertical shear-layer, which caused the spanwise transfer of low- and high-momentum fluids and then led to the generation of a $\delta$-scale secondary flow. Willingham *et al.* [17] stated that the LMP constitutes Prandtl's second kind of secondary flow. Anderson *et al.* [27] confirmed that this mean secondary flow is Prandtl's second kind of secondary flow, both driven and sustained by spatial gradients in the Reynolds-stress components, which cause a subsequent imbalance between production and dissipation of turbulent kinetic energy that necessitates secondary advective velocities. As Townsend [28] proposed, the large-scale secondary motions generated as previously mentioned could be sustained due to the transverse gradients of the imposed stress on the bounding surface. Recently, Xu *et al.* [29] investigated the development of a laminar boundary layer over a rectangular convergent-divergent riblet section in a water flume. They found that the fluid inside the riblet valley follows a helicoidal path and interacts with the crossflow playing an important role in determining the structure of the secondary flow. As Vanderwel *et al.* [24] anticipated, because these secondary flows have such a large impact on the structure of the boundary layer, and can be created easily by modifying the surface topology, these flows could have important consequences for near-wall mixing, drag reduction, and flow control. Therefore, it is informative to further investigate the characteristics of LSSVs generated by these control devices and the underlying mechanisms, as well as their effectiveness in suppressing boundary-layer separation.

Many experiments and numerical simulations have been devoted to spanwise heterogeneity control, but most of the research is limited to simple geometries, such as a flat plate boundary layer [8-10,16,17,24,26,30,31] or planar channel flow [22,25,29,32-34]. The study of spanwise-heterogeneity small-scale control in separated flows has never been reported to the authors' knowledge. In this paper, spanwise alternating distributed strips (SADS), composed of alternatively imposed out-of-phase control (OPC) and in-phase control (IPC) wall-normal velocity actuation, is applied to control flow past a backward-

facing rounded ramp. The control method was developed by Ni *et al.* [33,34] and they showed that LSSVs, whose scale can be up to the half-height of channel, could be generated by small-scale wall actuation. This paper aims to investigate SADS control in separated flow to assess the performance of this control strategy in suppressing flow separation, focusing on the fundamental mechanisms of the flow control. The active wall actuation, which is difficult to be implemented in practical application, is taken as an effective approach to realise the spanwise heterogeneities. The computational geometry under consideration is a turbulent flow over a backward-facing rounded ramp, which has been studied by Lardeau *et al.* [35] and Bentaleb *et al.* [36]. The simulations are carried out using implicit large-eddy simulation (ILES) at a Reynolds number of $Re$ = 7,106 (based on the freestream velocity and the height of the rounded ramp $H$) and at a low Mach number of $M$ = 0.2. A relatively low Reynolds number is considered to avoid the interactions between the outer-layer large-scale structures of a natural turbulent boundary layer as observed by Hutchins and Marusic [37] and the possible large-scale motions induced by SADS control. Four controlled cases with different widths of IPC/OPC strips are simulated in the present study to investigate the effect of the strip width, among which two cases are analysed in detail and optimised controlling parameters are finally suggested.

## II. METHODOLOGIES

The governing equations are described first, followed by an introduction of the numerical method and computational setup.

### A. Governing Equations

The three-dimensional (3-D) unsteady compressible Navier-Stokes (N-S) equations in a general, time-invariant system are solved numerically in a strong conservation non-dimensional form as,

$$\frac{\partial \boldsymbol{Q}}{\partial t} + \frac{\partial \boldsymbol{E}_i}{\partial x_i} = \frac{\partial \boldsymbol{F}_i}{\partial x_i} \tag{1}$$

In Eq. (1), $\boldsymbol{Q} = [\rho, \rho u, \rho v, \rho w, \rho e]^{\mathrm{T}}$ is the solution vector. The primary variables are the density $\rho$, the velocity components $u$, $v$ and $w$ and the total energy per unit mass $e$. The static temperature $T$ and pressure $P$ are related to the density $\rho$ via the equation of state of an ideal gas, $P = \frac{\rho T}{\gamma M^2}$. All the variables in the N-S equations are normalised by the reference parameters except additional descriptions. The N-S equations are non-dimensionalised with the reference density $\rho_{ref}$, the reference velocity $u_{ref}$, the reference temperature at the wall $T_{ref}$ and the dynamic viscosity $\mu_{ref}$ as well as the height of the rounded ramp $H$. The resulting dimensionless parameters are the Reynolds number $Re = \rho_{ref} u_{ref} H/\mu_{ref}$ and the Mach number $M = u_{ref}/\sqrt{\gamma R T_{ref}}$. A constant Prandtl number $Pr = \mu\, C_p/\kappa = 0.72$ is used, where $C_p = \gamma R/(\gamma - 1)$ is the specific heat capacity of gas at constant pressure and $\kappa$ is the thermal conductivity. The gas constant $R$ and the specific heat capacity ratio $\gamma$ are set to be $R = 287.1\, J/(Kg \cdot K)$ and $\gamma = 1.4$, respectively.

The convective vector, $\boldsymbol{E}_i$, and the diffusive vector, $\boldsymbol{F}_i$, in (1) are respectively expressed as

$$\boldsymbol{E}_i = \begin{bmatrix} \rho u_i \\ \rho u u_i + \delta_{1i} P \\ \rho v u_i + \delta_{2i} P \\ \rho w u_i + \delta_{3i} P \\ (\rho e + P) u_i \end{bmatrix} \qquad \boldsymbol{F}_i = \begin{bmatrix} 0 \\ \tau_{1i} \\ \tau_{2i} \\ \tau_{3i} \\ b_i \end{bmatrix} \tag{2}$$

with the standard Einstein summation notation. In the present paper, the following nomenclature is adopted. Indices *i*=1, 2, 3 correspond to the streamwise, wall-normal and spanwise directions, respectively. The notation $x_i = (x_1, x_2, x_3)$ is adopted to represent $(x, y, z)$ and $u_i = (u_1, u_2, u_3) = (u, v, w)$ corresponds to the streamwise, wall-normal and spanwise velocity components, respectively, and $\delta_{ij}$ is the standard Kronecker delta.

The total energy per unit mass *e* is expressed as

$$e = \frac{1}{2}(u_i u_i) + \frac{T}{\gamma(\gamma - 1)M^2} \tag{3}$$

The stress tensor and the heat flux vector are expressed as

$$\tau_{ij} = \frac{\mu}{Re}\left(\frac{\partial u_i}{\partial x_j} + \frac{\partial u_j}{\partial x_i} - \frac{2}{3}\delta_{ij}\frac{\partial u_k}{\partial x_k}\right) \tag{4}$$

and

$$b_i = u_j \tau_{ij} + \frac{\mu}{PrRe(\gamma - 1)M^2}\frac{\partial T}{\partial x_i} \tag{5}$$

The non-dimensional dynamic viscosity coefficient $\mu$ is calculated via the Sutherland law

$$\mu = T^{1.5}\frac{T_S + 1}{T + T_S} \tag{6}$$

where $T_S = \frac{110.4K}{293.15K} = 0.3766$.

### B. Numerical Method

An in-house CFD code ASTR, which has been applied to DNS [38,39] and LES [40] of boundary layer and channel flows, is used as the flow solver. The N-S equations are projected to the Cartesian coordinate system of the computational domain and solved by the high-order finite difference method.

All the spatial derivatives are approximated with a classic sixth-order compact central scheme [41]. The diffusive terms are also solved in conservative form, in which the second derivatives of the diffusive terms are solved by applying compact central finite-difference operators for the first derivative twice, which is more efficient than the direct calculation of second derivatives [42], although the latter method can be numerically more stable. To remove the small-scale wiggles due to aliasing errors resulting from discrete evaluation of the nonlinear convective terms, a tenth-order compact filter is adopted, which limits the filter only at high wavenumbers [43]. The filter also acts as like a subgrid-scale model by providing numerical dissipation

at the subgrid scales, and thus the use of an explicit subgrid-scale model can be avoided. As the explicit subgrid-scale models are usually derived from equilibrium turbulent flows, it might even lead to undesirable non-physical results in complex non-equilibrium flows [44, 45]. The approach adopted here is the ILES technique, which was first introduced by Visbal *et al.* [46-48] and proved to be effective in simulating controlled turbulent flows [49]. Once the spatial terms are solved, a third-order total variation diminishing Runge–Kutta method [50] is used for the time integration.

### C. Computational Setup

An ILES of the flow past a backward-facing rounded ramp is first performed as the baseline case. The geometry of the rounded ramp corresponds to the configuration in the LES study of Lardeau *et al.* [35] and Bentaleb *et al.* [36], as sketched in FIG. 1. The domain spans from $x$ = -30.0 to 25.0 in the streamwise direction. A rounded ramp step of height $H$ is attached to the flat plate at $x$ = 0.0. The SADS control is imposed onto the flat plate surface upstream of the rounded ramp from $x_{start} = -10.0$ to $x_{end} = 0.0$.

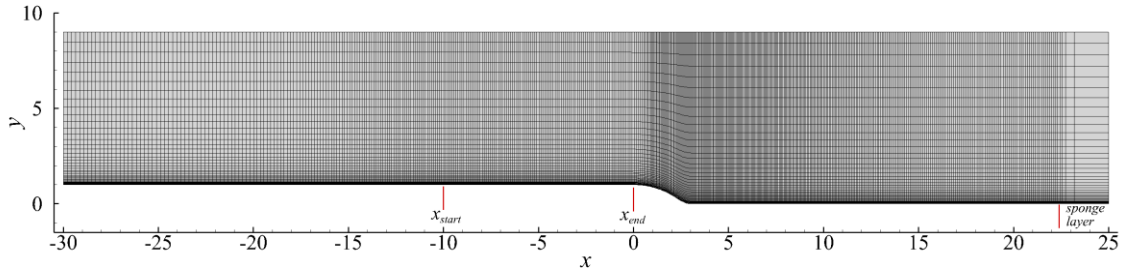


FIG. 1. Sketch of the computational domain and reduced numerical mesh. The mesh is plotted every 5th grid line in both $x$ and $y$ directions.

A diagram showing the SADS control layout is illustrated in FIG. 2 (a). The active wall-normal velocity at the wall surface imposed by the OPC and IPC, respectively, are given as

$$v_{wall}(x,z) = -A_{OPC}v(x,y_{dtc},z) \tag{7}$$

and

$$v_{wall}(x,z) = +A_{IPC}v(x,y_{dtc},z) \tag{8}$$

where $v_{wall}(x,z)$ is the wall-normal velocity at the wall. The coefficients $A_{OPC}$ and $A_{IPC}$ are the two parameters that control the amplitude of the wall velocity, which are both set to 0.5 in the present study to ensure the stability of the simulations. The detected position in wall viscous units $y_{dtc}^{+}$, ranges from 12 ($x = x_{start}$) to 15 ($x = x_{end}$), for the baseline case. Choi *et al.* [51] first introduced the OPC method into a turbulent channel flow where $A_{OPC}$ was set equal to 1.0. They observed a reduction in skin friction of ~25% on each wall at $y_{dtc}^{+} \approx 10$. Based on their study, Ni *et al.* [33,34] prescribed a fixed $y$-location of $y_{dtc}^{+} \approx 11$ in a SADS controlled turbulent channel flow, and their analysis suggested that the LSSVs can be generated and sustained by these small-scale control devices and the momentum transport across the channel is largely enhanced. A sketch of the control

method is presented in FIG. 2b. Stroh *et al.* [22] studied the change of the secondary motion topology with the width of the free-slip regions by restricting the spanwise wavelength of the no-slip/free-slip region. Similar to their parametric study, the centre-to-centre spacing between two neighbouring OPC/IPC strips keep constant as the half of the computational domain width $0.5L_z$, *i.e.* $L_{IPC} + L_{OPC} = 0.5L_z$. Four controlled cases with different IPC/OPC width are studied, and the widths of IPC strips are summarised in TABLE I.

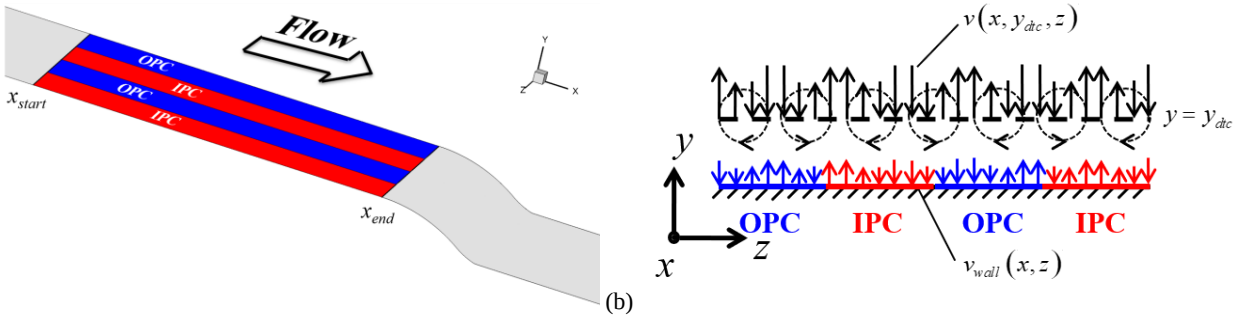


(a) (b)

FIG. 2. (a) Sketch of the topography configuration for equal spanwise width of OPC and IPC strips and (b) schematic of the control method used in the present study. The SADS control is imposed onto the flat plate surface upstream of the rounded ramp from $x_{start} = -10.0$ to $x_{end} = 0.0$. The regions of OPC and IPC are denoted by blue and red strips respectively in (a). The black and coloured arrows represent the wall-normal velocity at the detected position and the wall respectively in (b).

TABLE I. Summary of the ILES cases in the present study

| Case | $L_{IPC}$ | $L_{IPC}^{+}$ [a] |
|---|---|---|
| NC | Baseline case with no control | |
| W4 | $0.4H$ | 124 |
| W5 | $0.5H$ | 155 |
| W7 | $0.7H$ | 217 |
| WE | $1.25H$ | 387 |

[a] $L_{IPC}^{+}$ refers to $L_{IPC}$ normalised by the wall viscous length scale of Case NC at $x_{start}$.

For all the cases studied, the reference Reynolds number is set to $Re$ = 7,106. The Reynolds number based on nominal thickness $\delta$, displacement thickness $\delta^*$ and momentum thickness $\theta$ of the boundary layer as well as the friction Reynolds number $Re_\tau$ at $x = x_{start}$ are given in TABLE II. The reference Mach number is $M$ = 0.2, defining a weakly compressible boundary layer. The size of the computational domain in the streamwise and spanwise directions is $L_x \times L_z = 55 \times 5$ and for the wall-normal direction, $L_y$ changes from 8 (upstream of the rounded ramp) to 9 (downstream of the rounded ramp). The computational domain is discretised with a mesh of $1290 \times 200 \times 300$ nodes in the streamwise, wall-normal and spanwise directions, respectively. As shown in FIG. 1, the mesh is refined above the rounded ramp as well as its neighbouring upstream and downstream regions along the streamwise direction, stretched towards the walls in the wall-normal direction and evenly distributed in the spanwise direction. The mesh resolution at $x = x_{start}$ in local wall unites is also presented in TABLE II. More analysis on the mesh resolution can be found in Appendix. The time step of the computation $\Delta t$ is $4.5 \times 10^{-4}$. It

corresponds to $\Delta t^+ = 3.2 \times 10^{-3}$ normalised by the viscous time scale $t_\tau = \frac{l_\tau}{u_\tau}$, where $l_\tau = \frac{\mu_w}{\rho_w u_\tau}$ is the wall viscous length scale calculated by the wall units of the baseline case at $x_{start} = -10.0$.

TABLE II. Boundary layer parameters and mesh resolution at $x = x_{start}$

| $x$ | $Re_\delta$ [a] | $Re_{\delta^*}$ [a] | $Re_\theta$ [a] | $Re_\tau$ [b] | $\Delta x^+$ | $\Delta y_1^+ \sim \Delta y_\delta^+$ | $\Delta z^+$ |
|---|---|---|---|---|---|---|---|
| $x_{start}$ | 14910 | 1715 | 1120 | 650 | 13.2 | 0.66~9.0 | 5.2 |

[a] $Re_\delta$, $Re_{\delta^*}$ and $Re_\theta$ refer to the Reynolds number based on nominal thickness $\delta$, displacement thickness $\delta^*$ and momentum thickness $\theta$, respectively.

[b] The friction Reynolds number $Re_\tau$ is calculated via $Re_\tau = \frac{\rho_w u_\tau \delta}{\mu_w}$ based on the wall friction velocity $u_\tau$ at $x_{start}$, where $u_\tau$ is defined as $u_\tau = \sqrt{\frac{\tau_w}{\rho_w}}$, and $\tau_w = \mu_w \frac{\partial u}{\partial y}\Big|_w$ is the local wall shear stress.

A no-slip isothermal boundary condition is applied to the wall as $T_w = T_{ref}$. The digital filter method proposed by Touber and Sandham [54] is used to generate synthetic inflow turbulence and a transitional region of $18\delta_{start}$ is incorporated to let synthetic fluctuations evolve into fully developed turbulence, where $\delta_{start}$ is the boundary-layer thickness at $x = x_{start}$. Morgan *et al.* [55] suggested that the flow reaches equilibrium status around $x/\delta_r = 10.6$ in a turbulent-boundary layer developing over an adiabatic flat plate using digital filter method, where $\delta_r$ is the boundary-layer thickness at the reference location. The generated artificial turbulent fluctuations are superimposed onto the turbulent mean velocity and temperature profiles and introduced to the computational domain via the inflow boundary condition applied at $x = -30.0$. At the upper and outlet planes, generalised non-reflecting boundary conditions [56,57] are used. Sponge layers are applied at the outlet ($x = 21.7$) to filter the outgoing waves. Periodic boundary conditions are prescribed in the spanwise direction.

For the baseline case, after the transient period, the flow becomes fully turbulent and reaches a statistically steady state after about 133 time units. After the imposition of the SADS control, the flow undergoes another transient period of around 70 time units before reaching a statistically steady state. For all the cases, the data samples are collected for at least 100 time units before being post-processed and analyzed.

## III. RESULTS AND DISCUSSIONS

In Section III.A, the results are first validated by comparing the baseline (denoted by Case NC) with the incompressible DNS database of Schlatter and Örlü [58] and Jiménez *et al.* [60]. Then, the turbulence coherent structures visualised by the iso-surfaces of the *Q* criterion are presented for all the cases in Section III.B to illustrate the impact of SADS control on the turbulence intensity. It is followed by further analysis of the mean flow field data to study the influence of the strip width on the mean statistics, including the skin friction coefficient $C_f$, the pressure coefficient $C_p$, the skin friction lines, the streamwise velocity profiles and the variation of the mean streamwise velocity in the *y*-*z* plane. We will demonstrate that Case W5 presents

the best control performance regarding the flow reattachment and the largest delay of the flow separation is obtained by Case WE, and these two cases are analysed in detail in Section III.C.

### A. Validation

To validate the numerical method, the mean velocity profile of the baseline case, normalised by the local friction velocity $u_\tau$ in the equilibrium zone ($x = x_{start}$), is compared with the classic law of the wall and the incompressible DNS data of Schlatter and Örlü [58] in FIG. 3. In the present paper, " $\bar{}$ " and $\langle\ \ \rangle$ stand for the time- and space-averaged operators, respectively, *i.e.* $\langle\ \ \rangle_z$ is used for the spanwise averaged variables. The fluctuations from each averaged operator are defined as $g' = g - \bar{g}$ and $g_{\langle z\rangle} = g - \langle g\rangle_z$, where $g$ is a generic variable. The averaged operators can be combined as they are both linear operators, *i.e.* $\langle\bar{g}\rangle_z$ and $g'_{\langle z\rangle}$ might be used, for instance. According to FIG. 3, good agreement between the present ILES result and the DNS data of Schlatter and Örlü [58] is obtained and the difference in the wake layer is attributed to Reynolds number effects [59].

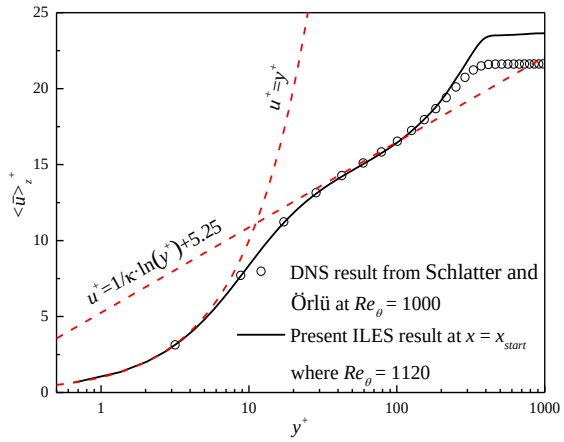


FIG. 3. Mean velocity profile normalised by the local friction velocity. The von Kármán constant is κ=0.41.

The root mean square (RMS) velocity fluctuations $u'_{i,rms} = \sqrt{\langle\overline{u'_{i,\langle z\rangle}u'_{i,\langle z\rangle}}\rangle_z}$ ($i$=1, 2, 3) and the Reynolds shear stress (RSS) in the equilibrium zone of the baseline case are compared with the DNS data of Schlatter and Örlü [58] and Jiménez *et al.* [60] in FIG. 4. A general good agreement for the RMS velocity fluctuations and the RSS are observed in the near-wall region. However, high values of velocity fluctuations can be seen in the outer part of the boundary layer for the baseline case, which is a common phenomenon observed in simulations of turbulent boundary layers using artificial inflow turbulence technologies [54, 55].

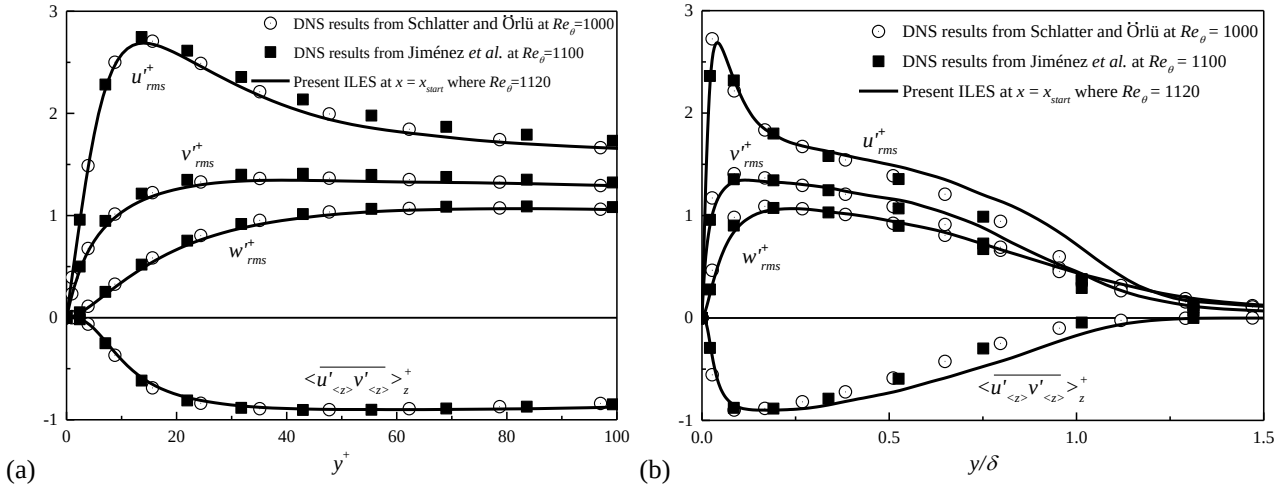


(a) (b)

FIG. 4. RMS velocity fluctuations and Reynolds shear stress in inner scaling (a) and outer scaling (b).

## B. General Properties of the Flow Fields

The turbulence coherent structures above the backward-facing rounded ramp and its neighbouring upstream and downstream regions, identified by the iso-surfaces of the $Q$ criterion [62] ($Q = 4\left(u_{ref}/H\right)^2$ in FIG. 5) and coloured by the instantaneous streamwise velocity $u$, are presented in FIG. 5 for all cases. Compared with the baseline case, the turbulence coherent structures of cases with SADS are alternatively redistributed over the controlled region. In general, these turbulence coherent structures are enhanced above the IPC strips, whereas above the OPC strips, a suppression of the coherent structures can be observed. The flow field above the controlled zone demonstrates a phase-locked reorganisation in correspondence with the topography configuration of the SADS distribution. The alternatively modified coherent structures above OPC/IPC strips exhibit the same tendency as those in turbulent channel flows controlled by SADS [33,34], indicating the evidence of suppression/enhancement of local turbulence. Furthermore, the alternating distributed suppressed and enhanced turbulence coherent structures can extend to the downstream of the controlled area, which is more distinct in the case with wider width of IPC strips (Case WE), as illustrated in FIG. 5 (c). More detailed quantitative analysis of the cases controlled by SADS will be shown in the next section and compared to the baseline case.

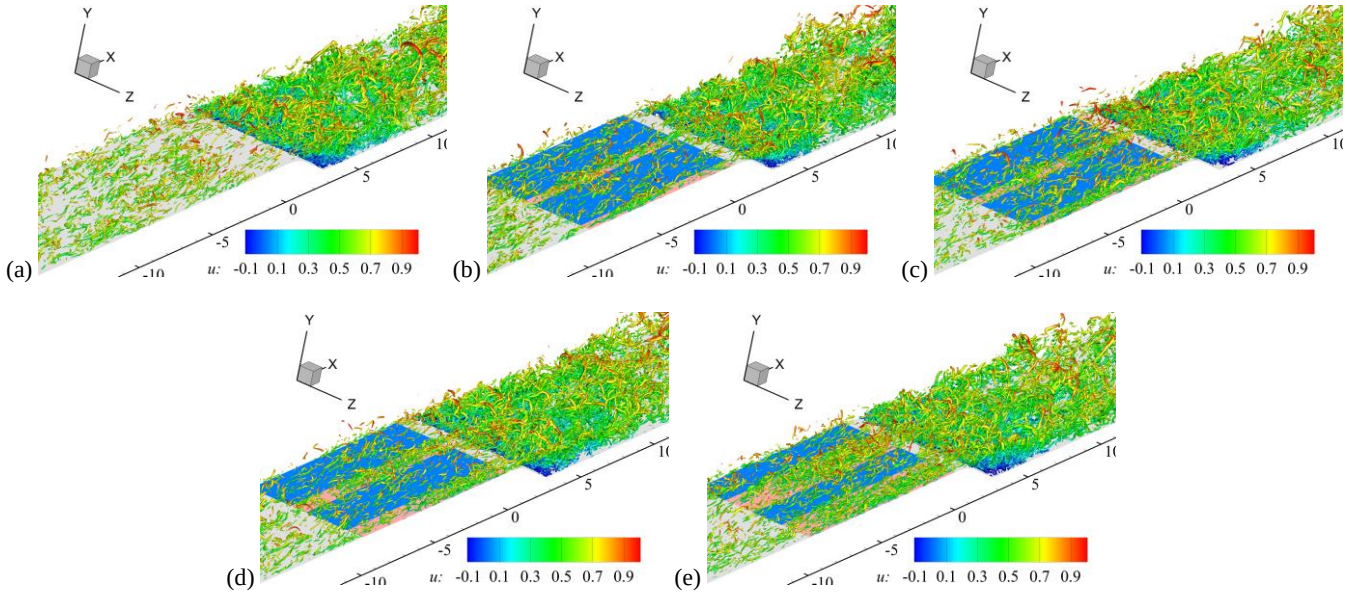


FIG. 5. Turbulence coherent structures visualised with iso-surfaces of $Q$ criterion and colored by instantaneous streamwise velocity $u$. The strips colored by blue and red on the wall upstream of the rounded ramp represent OPC and IPC regions respectively. (a) Case NC; (b) Case W4; (c) Case W5; (d) Case W7; (e) Case WE.

The mean statistics are analysed in detail in the following. The streamwise variation of the skin friction coefficient and pressure coefficient are firstly dealt with based on their respective spanwise- and time-averaged statistics and presented in FIG. 6. The mean skin friction coefficient $C_f$ and pressure coefficient $C_p$ are defined as,

$$C_f(x) = \frac{\mu_w \partial \langle \bar{u} \rangle_z / \partial y|_w}{\frac{1}{2}\rho_\infty u_\infty^2}, \tag{9}$$

and

$$C_p(x) = \frac{\langle \bar{P} \rangle_z - P_\infty}{\frac{1}{2}\rho_\infty u_\infty^2}. \tag{10}$$

where the subscript "$\infty$" refers to the incoming free-stream flow. It can be seen from FIG. 6 (a) that the near-wall flow upstream of the rounded ramp undergoes an acceleration and thus the skin friction coefficient reaches a peak just before the rounded ramp starts. This is due to the pressure drop induced by the convex curvature further downstream and the elliptic feature of the pressure field [36], as shown in FIG. 6 (b). For the controlled cases, the SADS control causes an increase in the skin friction upstream of the rounded ramp, due to the intense activation of turbulence locally by the IPC strip, which is consistent with the previous studies of channel flow [33, 34]. Accordingly, the skin friction upstream of the rounded ramp for the controlled cases increases with the width of the IPC strips monotonically. Case WE shows the highest skin friction upstream of the rounded ramp among all cases studied and this can be attributed to its widest width of the IPC strip.

After reaching the rounded ramp, the flow decelerates because of the adverse pressure gradient and separation occurs. The separation and reattachment locations, the length of the separation zone as well as the percentage reduction in the length of the separation zone in comparison with the baseline case for all cases studied are summarised in TABLE III. It can be seen from the zoomed left-hand-side sub-figure in FIG. 6 (a) and TABLE III that the time- and spanwise-averaged separation locations for the cases with SADS control vary monotonically with the width of the IPC strips and the best performance with regards to the separation delay is obtained by Case WE, whose IPC strips are the widest. It is because the enhanced turbulence above the IPC strips goes downstream and then increases the momentum transport of the corresponding downstream region, leading to the delay of separation. Since Case WE has the widest IPC strips among all the controlled cases, it leads to the biggest delay of the separation point. This assumption can be verified in FIG. 7, which shows the contours of distance of the $\bar{u} = 0$ plane projected onto the *x*-*z* surface. The white lines on the left-hand-side of the figures represent the separation lines while the right-hand-side white lines refer to reattachment lines. The blue (resp. red) strips plotted beside the *z*-coordinate axis in FIG. 7 (b)-(e) represent the regions controlled by OPC (resp. IPC). It can be observed that the separation locations downstream of the IPC strips are postponed whilst the separation positions are slightly shifted upstream in the limited regions downstream of the OPC strips, thus leading to an overall delay of separation. It can also be seen from FIG. 7 (b)-(e) that the regions where the flow separation is delayed are proportional to the width of the IPC strips. This is consistent with the separation locations summarised in TABLE III that the largest separation delay is observed by Case WE, which has the widest width of the IPC strips. Further downstream of the rounded ramp, the flow reattaches at $x = 5.03$ for the baseline case. However, after SADS control is imposed, the flow shows a better performance regarding the reattachment location and Case W5 behaves the best among the four controlled cases under consideration. The shortest length of separation zone is also achieved by Case W5 and the percentage of reduction in the length of the separation zone in comparison with the baseline can be 8.49%, as shown in TABLE III. Since much lower skin friction is induced by Case W5 upstream of the rounded ramp, it is the optimal one among all the cases studied to suppress the flow separation. It can be seen from FIG. 6 (b) that there exists a pressure plateau within the separated near-wall region for the baseline case whilst this plateau is lifted up after imposing SADS control, especially for Case WE. This indicates that the control method adopted in the present study increases the pressure in the recirculation zone and plays a positive role in reducing pressure drag.

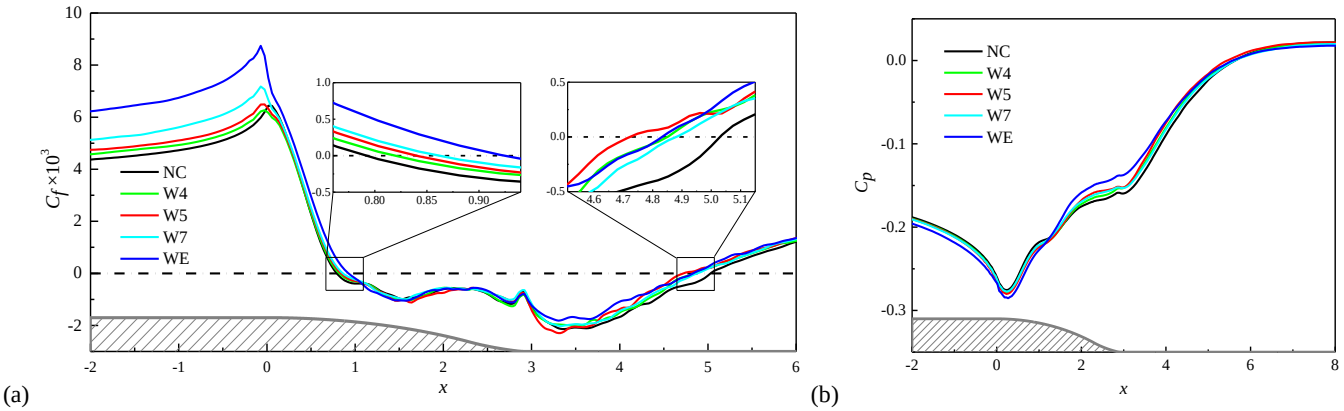


FIG. 6. Skin friction coefficient $C_f$ (a) and pressure coefficient $C_p$ (b) based on spanwise- and time-averaged flow field. The grey line at the bottom of the figure and its underneath filled area represent the shape of the geometry adopted in the present study.

TABLE III. Summary of separation zone the characteristics regarding the flow separation and reattachment for all the cases

| Case | Separation location | Reattachment location | Length of the separation zone | Percentage of reduction in the length of the separation zone |
|---|---|---|---|---|
| NC | 0.79 | 5.03 | 4.24 | / |
| W4 | 0.82 | 4.85 | 4.03 | 4.95% |
| W5 | 0.84 | 4.72 | 3.88 | 8.49% |
| W7 | 0.86 | 4.88 | 4.02 | 5.19% |
| WE | 0.92 | 4.83 | 3.91 | 7.78% |

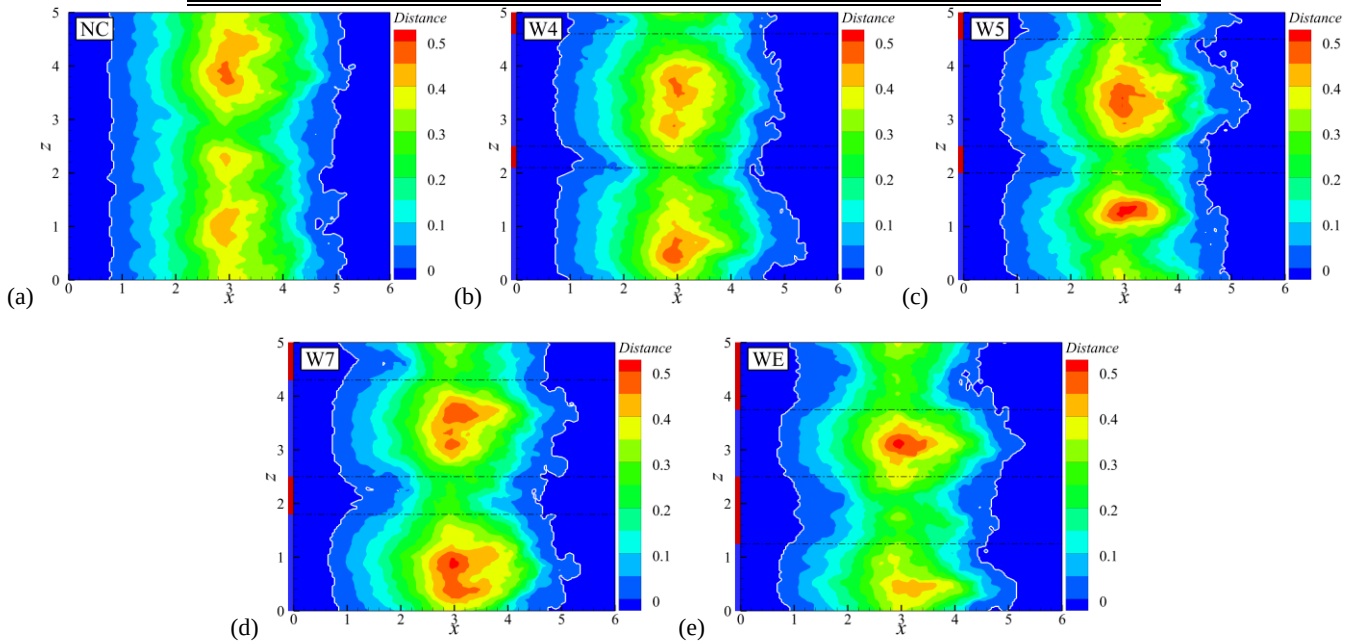


FIG. 7. Distance between the contour line of the time-averaged streamwise velocity $\bar{u} = 0$ and the wall. The white lines on the left side of the figures show the separation lines while those right-hand-side white lines refer to reattachment lines. The blue and red strips plotted beside the $z$-coordinate axis in (b) and (c) represent the regions controlled by OPC and IPC respectively. The dash-dot lines divide the regions following the extension lines of the interface between the OPC and IPC strips upstream of the rounded ramp. (a) Case NC; (b) Case W4; (c) Case W5; (d) Case W7; (e) Case WE.

The distribution of the skin friction coefficient and the skin friction streamlines, for all the cases calculated by the time-averaged statistics, are plotted in FIG. 8. In general, the skin friction coefficient increases over the IPC strips due to the increase in the local turbulence intensity. The spanwise variations of the time-averaged skin friction coefficient at $x = 0.0$ upstream of

the rounded ramp are given in FIG. 9 to quantify the effect of both the OPC and IPC strips. It can be seen that the skin friction coefficient is reduced over the OPC strips whereas it rises to a large extent over the IPC strips. Similar spanwise distribution of the skin friction coefficient for the controlled cases was also observed in the SADS controlled turbulent channel flow [33,34]. However, a much more distinct decrease of the skin friction over the OPC strips is obtained compared with those in the channel flow. A similar level of increase for all the controlled cases with regards to the spanwise-averaged value of $C_f(z)\big|_{x=0.0}$ above the IPC strips can be seen in FIG. 9. This is independent of the IPC strip width and differs from the spanwise variation of the skin friction coefficient in the SADS turbulent channel flow case where a clear maximum increase above the IPC strips is obtained by the case with 2 pairs of equal-width strips (Case Nstrip4) [33], whose width is $\Delta z^+ = 264$ based on the friction velocity of the baseline case. As reported by Mejia-Alvarez *et al.* [9], the abrupt wall stress variation would induce transverse turbulent mixing which is the source of a $\delta$-scale secondary flow. Therefore, the spanwise heterogeneities of skin friction generated by SADS control would induce large-scale streamwise structures. The skin friction lines for all the cases are plotted in FIG. 8 to describe the 3-D flow structures. The critical point theory [63] focusing on the skin-friction lines can be used to study 3-D structures near the reattachment locations. A critical point can be of three types: a node, saddle or focus. For the controlled cases, a distinct node around the separation line can be observed downstream of the IPC strips whereas a saddle is seen between the neighbouring nodes downstream of the OPC strips, as illustrated in FIG. 8 (b)-(e). The flow topology of the controlled cases is reorganised by alternatively distributed OPC and IPC strips. It is shown in FIG. 8 (a) that 5 nodes around the reattachment line can be recognized in Case NC whereas the number of the nodes in the corresponding region is reduced to 4, 3, 4, 3 for Cases W4, W5, W7 and WE, respectively. It indicates that the spanwise spacing of the neighbouring nodes is increased by SADS control, suggesting larger flow structures are dominating the flow reattachment. This should be the main mechanism of the control method in improving the performance of flow reattachment. It can be seen that the number of the nodes around the reattachment line in Cases W5 and WE is less than that in Cases W4 and W7, suggesting larger flow motions are in the former two cases. Consequently, better control effects are obtained with regards to the reattachment locations, as summarised in TABLE III.

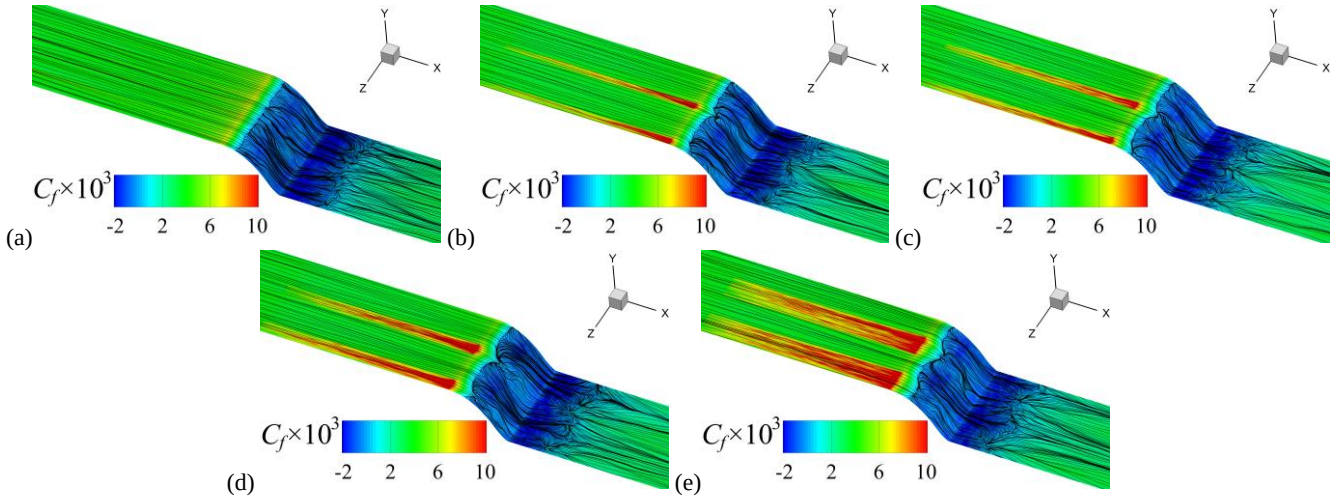


FIG. 8. Time-averaged skin friction coefficient and skin friction lines. (a) Case NC; (b) Case W4; (c) Case W5; (d) Case W7; (e) Case WE.

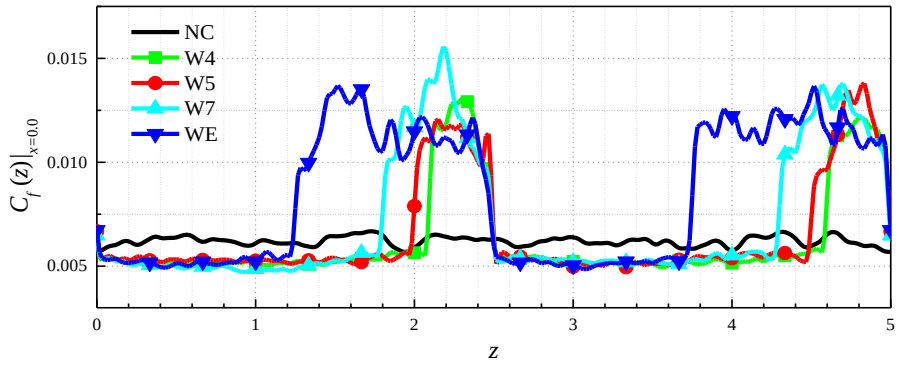


FIG. 9. Mean skin friction coefficient $C_f(z)\big|_{x=0.0}$ based on time-averaged statistics.

The distribution of the mean streamwise velocity $\langle\bar{u}\rangle_z$, normalised by the reference velocity $u_{ref}$, obtained from the turbulent boundary-layer flow upstream of the separation bubble through to the reattached flow region, are presented in FIG. 10. The zero-streamwise-velocity locations are shown as dash-dot white lines for all the cases on the left-hand-side of FIG. 10 whereas they are represented by dash-dot black line and solid red lines for the baseline case and the controlled cases, respectively, on the right-hand-side of FIG. 10. The black and red solid circles in FIG. 10 (j) represent the inflection points of the mean streamwise velocity profiles for the baseline case and the controlled case, respectively. These zero-streamwise-velocity locations bisect the recirculation zone as mentioned in Bentaleb *et al.* [36]. Compared with Case NC, the SADS control acts positively to suppress the flow separation for all cases. The size of the recirculation zone is reduced by SADS control although the spanwise variation of the separation bubbles in the spanwise direction are enhanced, as indicated in FIG. 7 (b)-(e). It can be seen from FIG. 7 (b)-(e) that, for all the controlled cases, the height of the separation bubble downstream of the IPC strips decreases whilst a relatively larger separation zone is obtained downstream of the OPC strips. Among all the controlled cases, Case W5 shows a more effective influence on the second half of the recirculation zone and Case WE exhibits the best control effect on the first half of the separated flow. The mean streamwise velocity profiles, located at $x$ = 0.0, 0.8, 1.5,

2.0, 2.5, 3.0, 4.0, 5.0 and 5.5, are plotted on the right-hand-side of FIG. 10. This allows a quantitative comparison of the evolution of the flow separation, reattachment and flow recovery to equilibrium status between the baseline case and the controlled cases. It can be observed from Case WE (FIG. 10 (j)) that the near-wall flow is accelerated under the inflection point of the velocity profile in the recirculation zone after imposing SADS control whereas the velocity in the outer part of the free shear-layer slightly decreases compared with Case NC. This indicates that there exist large-scale structures in the controlled case, which enhances the momentum transport between the main flow and the separated flow since the inflection point of the streamwise velocity profile can be regarded as the edge of the recirculation zone. Therefore, the separated flow in the controlled case has great potential to realise the reattachment shifting upstream. It can also be observed in FIG. 10 (j) that the inflection points for Case WE shift towards the wall compared with those from the baseline case, demonstrating that the flow separation is effectively suppressed by SADS control. Based on the above analysis, since Case W5 presents the best control performance on the flow reattachment and the largest delay of the flow separation is obtained by Case WE, these two cases will be analysed in detail.

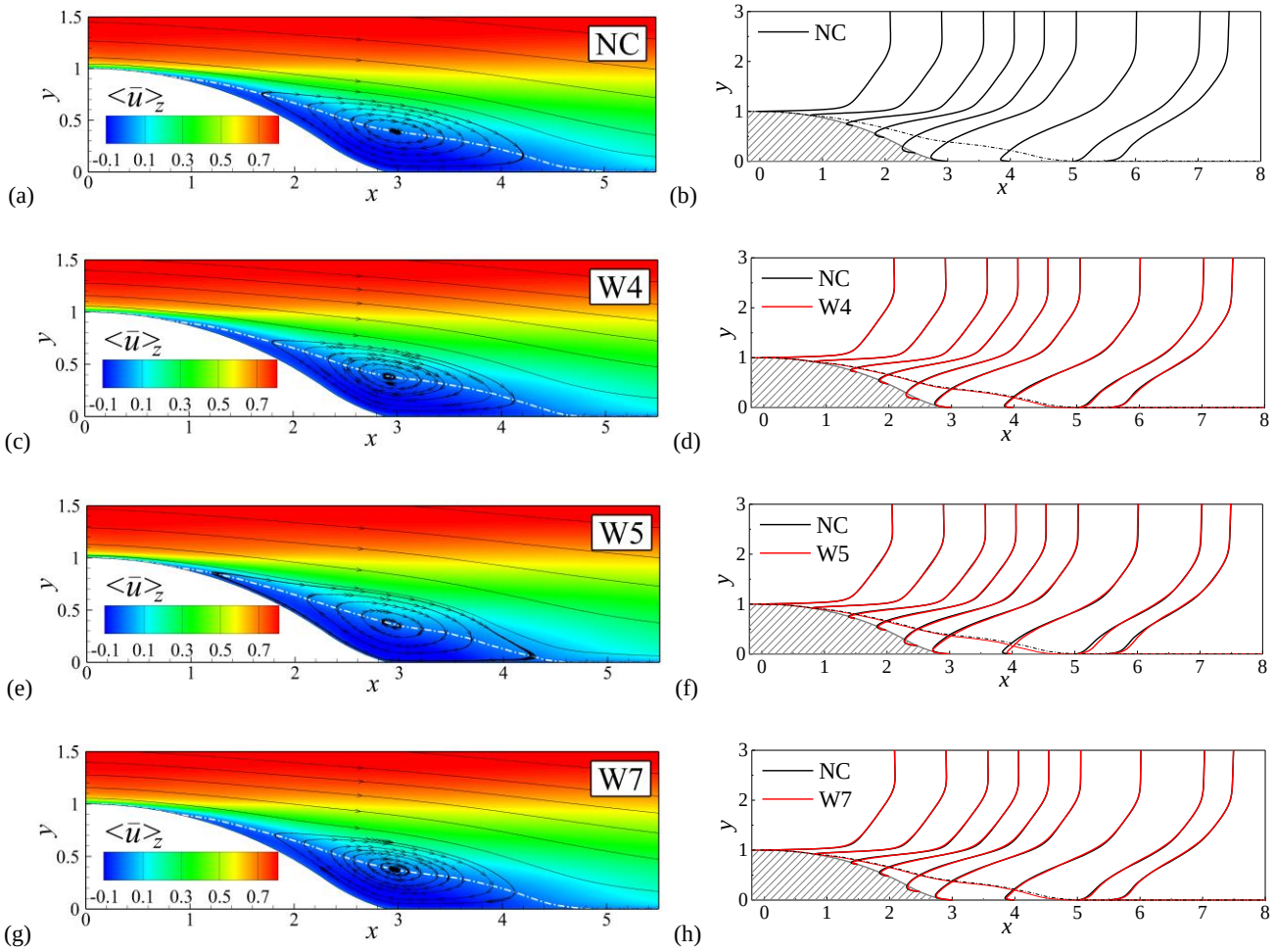

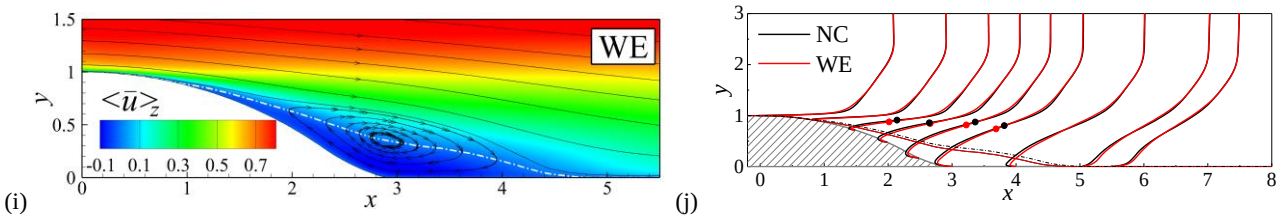


(i) (j)

FIG. 10. Distribution of the mean streamwise velocity $\langle \bar{u} \rangle_z$ in outer scaling normalised by reference velocity (left-hand-side) and its profiles at $x$ = 0.0, 0.8, 1.5, 2.0, 2.5, 3.0, 4.0, 5.0 and 5.5 (right-hand-side). The zero-streamwise-velocity locations are shown as dash-dot white lines for all the cases on the left-hand-side whereas they are represented by dash-dot black line and solid red lines for the baseline case and the controlled cases, respectively, on the right-hand-side. The black and red solid circles in (j) represent the inflection points of the mean streamwise velocity profiles for the baseline case and the controlled case, respectively. The results come from Case NC, Case W4, Case W5, Case W7 and Case WE from top to bottom.

## C. Comparative analysis of Cases NC, W5 and WE

### a. Mean Flow

The mean streamwise velocity fields $\bar{u}$ in the $y$-$z$ plane of Cases NC, W5 and WE selected from $x$ = 0.0, 0.8, 2.0, 3.0, 4.0, 5.0 are compared in FIG. 11 to show the spanwise variation of the mean streamwise velocity in the separation zone. The zero-streamwise-velocity locations are shown as dash-dot white lines for all the cases. The blue and red strips with black borders plotted under the $z$-coordinate axis represent the corresponding regions downstream of the flat plate surface controlled by the OPC and IPC strips, respectively. It can be seen from FIG. 11 (b) and (c) that the flow field at the beginning of the rounded ramp ($x = 0$) is reorganized by Case W5 and WE compared with the baseline case in FIG. 11 (a). A transverse movement of fluid is induced in the controlled cases between the neighbouring downstream of OPC and downstream of IPC strips. As observed in FIG. 11 (e) and (f), around the separation point of Case NC, the near-wall velocity increases above the wall downstream of IPC region whereas large-scale low-speed regions are induced above the wall downstream of OPC strips. The accelerated fluid above the wall downstream of IPC regions play a critical role in delaying the flow separation as the ability of the fluid to resist flow separation is enhanced. This has been verified in FIG. 7 (b) and (c) that flow above the wall downstream of IPC regions separates later than that over the wall downstream of OPC strips. Therefore, a reasonable interpretation is that the wider the IPC strips are, the better the delay of the flow separation works. This is also consistent with the mean separation locations summarised in TABLE III, showing that Case WE exhibits the best separation delay. Further, it can be seen from FIG. 11 (i), (l) and (o) that the height of the separation bubble is reduced above the wall downstream of IPC strips whereas in the limited regions over the wall downstream of OPC strips, the recirculation zone enlarges in the wall-normal direction. This suggests that the control method adopted in the present research takes a prominent role in suppressing flow separation. The zero-streamwise-velocity locations calculated by time- and $z$-averaged statistics illustrated in FIG. 10 (f) show consistent results. For Case W5 in the corresponding streamwise position (as indicated in FIG. 11 (h), (k) and (n)), the positive effects exerted on the flow field extend to the neighbouring downstream of OPC strips, especially for those located at the left-hand-side of

downstream of IPC strips. This differs from the approximate phase-locked variation of the mean streamwise velocity imposed by Case WE. In the reattachment region of Case WE, as indicated in FIG. 11 (q) and (r), spanwise alternating distributed low- and high-velocity regions can be observed, similar to the observation in channel flow with SADS control [33,34]. Therefore, the large-scale structures are induced by the alternating distributed OPC and IPC strips upstream of the rounded ramp, and they can be sustained downstream of the rounded ramp and interact with the separation bubble and the reattachment flow.

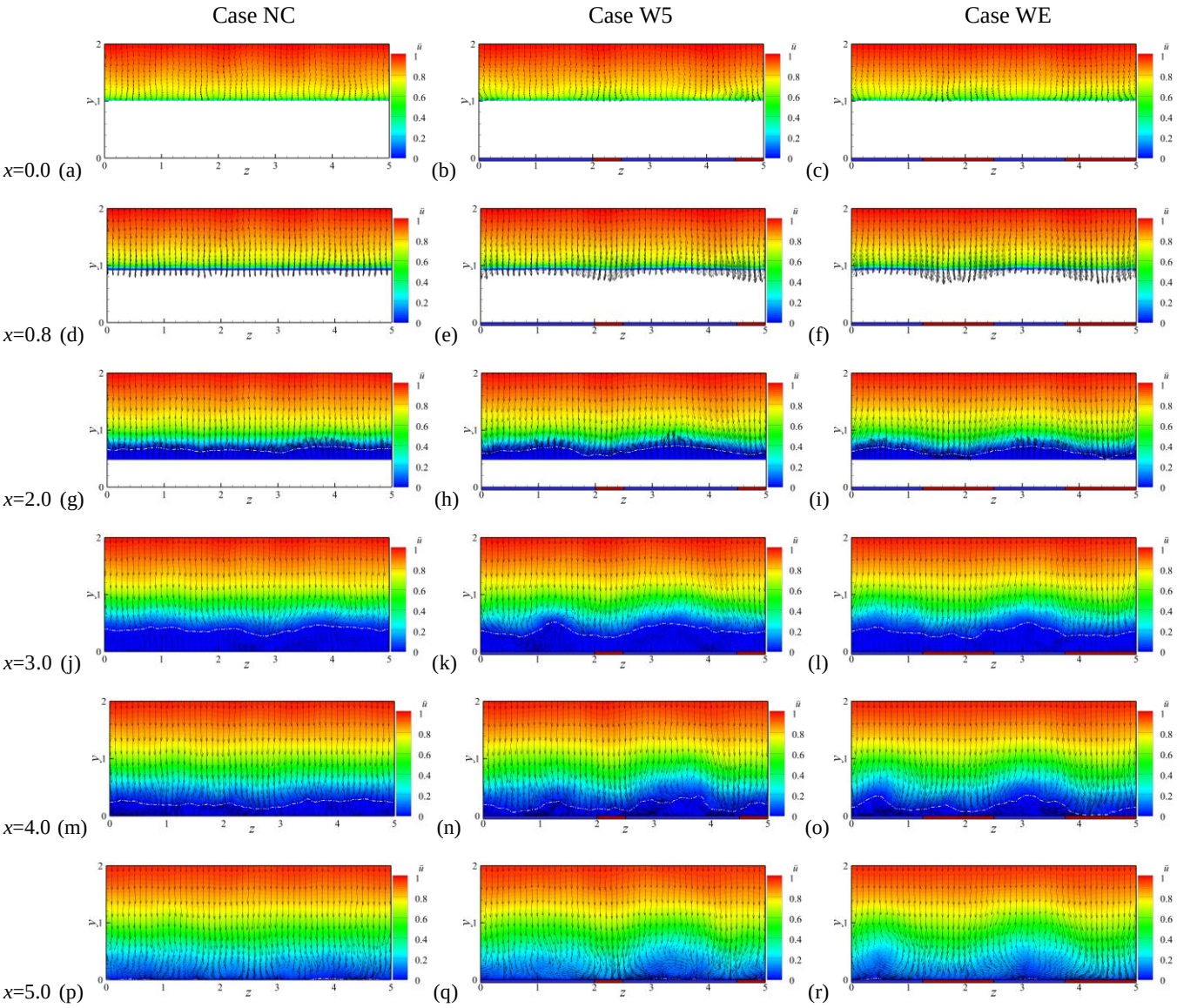


FIG. 11. Time-averaged streamwise velocity $\bar{u}$ as well as mean velocity vector $(\overline{w}, \overline{v})$ of Cases NC, W5 and WE from the left-hand-side to the right-hand-side respectively. The results come from $x$ = 0.0, 0.8, 2.0, 3.0, 4.0 and 5.0 from top to bottom. The zero-streamwise-velocity locations are shown as dash-dot white lines for all the cases. The blue and red strips with black borders plotted under the $z$-coordinate axis represent the corresponding regions downstream of the flat plate surface controlled by the OPC and IPC strips respectively.

### b. Reynolds Stress

The TKE and RSS, normalised by square of the reference velocity, are presented in FIG. 12 at nine streamwise locations ranging from $x$ = 0.0 to $x$ = 5.5 (before the detachment and after the reattachment). They are calculated with time- and $z$-averaged statistics as,

$$TKE|_{zt} = \frac{1}{2}\langle\overline{(u_k - \langle\overline{u_k}\rangle_z)(u_k - \langle\overline{u_k}\rangle_z)}\rangle_z / u_{ref}^2 \quad (k = 1,2,3) \tag{11}$$

and

$$RSS|_{zt} = \langle\overline{(u - \langle\overline{u}\rangle_z)(v - \langle v\rangle_z)}\rangle_z / u_{ref}^2 \tag{12}$$

where "$|_{zt}$" represents the fluctuation calculated by subtracting the $z$- and time-averaged velocity from the instantaneous one. The distribution of the $TKE|_{zt}$ and $RSS|_{zt}$ at six representative streamwise positions ($x$ = 0.0, 0.8, 2.0, 3.0, 4.0, 5.0) are zoomed in FIG. 13. It can be seen from FIG. 12 (a) and FIG. 13 (a) that before the flow reaches the separation point, the $TKE|_{zt}$ of Cases W5 and WE increase within the region of $y$ = 1.6 in comparison with the baseline case. Between the two controlled cases, Case WE exhibits a better performance in enhancing the near-wall turbulence energy, leading to a stronger extent of downstream separation delay. In the outer part of the boundary layer (For Cases NC, W5 and WE, the local boundary-layer thickness is comparable to the height of the rounded ramp.), a slight reduction of $TKE|_{zt}$ can be observed for both the controlled cases, and a further loss in the wall-normal direction is seen in Case WE as more turbulence energy is transported into the near-wall region. It can be seen that the variation of $RSS|_{zt}$ in FIG. 13 (a) is similar to that of $TKE|_{zt}$. The similar distribution of $TKE|_{zt}$ and $RSS|_{zt}$ for Cases NC, W5 and WE can be maintained until $x$ = 1.5, as illustrated in FIG. 12. Higher levels of $TKE|_{zt}$ and $RSS|_{zt}$ have a major contribution to the delay of flow separation. Inside the separation bubble, $TKE|_{zt}$ and $RSS|_{zt}$ are still higher for the controlled cases at $x$ = 2.0 due to the upstream effect. After flowing through the central part of the separated region ($x$ = 3.0), $TKE|_{zt}$ and $RSS|_{zt}$ of Case WE in the inner part of the boundary layer are gradually becoming smaller than those of Case NC, but in the outer part of the boundary layer, both $TKE|_{zt}$ and $RSS|_{zt}$ are still higher than those of the non-controlled case, due to the existence of LSSVs in the free shear-layer. Compared with Case WE, the $RSS|_{zt}$ of Case W5 still retains higher in the free shear-layer, leading to a stronger momentum transport between the main flow and separated flow, and a faster flow reattachment are therefore obtained. The control effects exerted on the spanwise variation of $TKE|_t$ and $RSS|_t$ are analysed next.

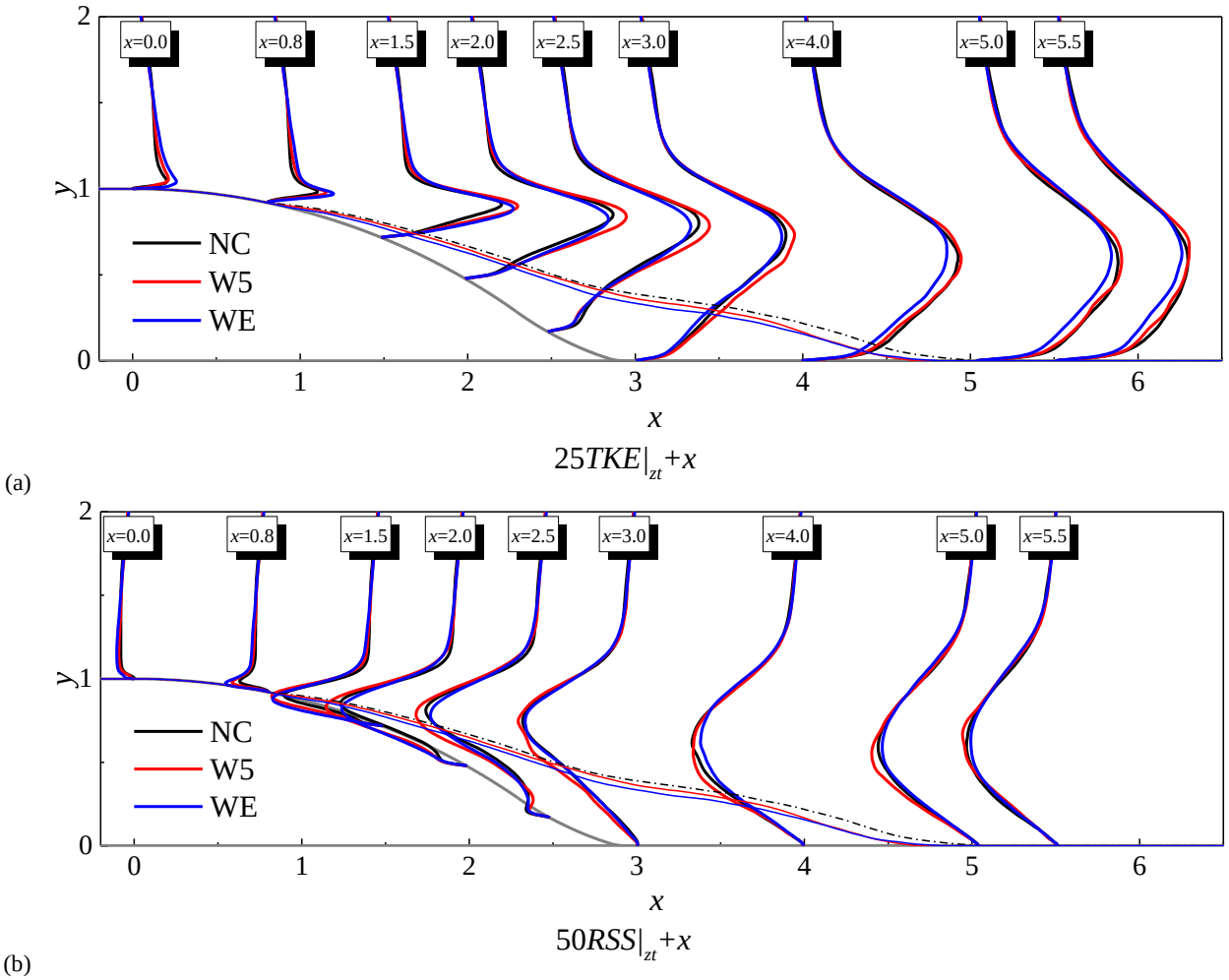


FIG. 12. (a) TKE and (b) RSS calculated by time- and $z$-averaged statistics for Cases NC, W5 and WE at $x$ = 0.0, 0.8, 1.5, 2.0, 2.5, 3.0, 4.0, 5.0 and 5.5. The zero-streamwise-velocity locations are shown as a dash-dot black line, solid thin red and blue lines for Cases NC, W5 and WE respectively. Note that scaling multipliers are used to simply gain an equally clear view of the variations for all quantities.

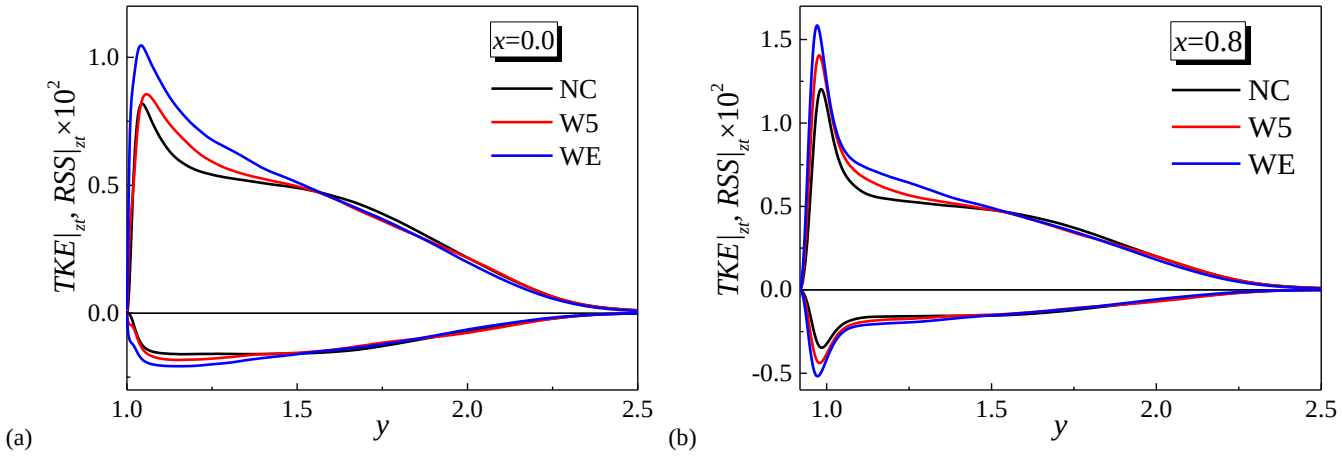

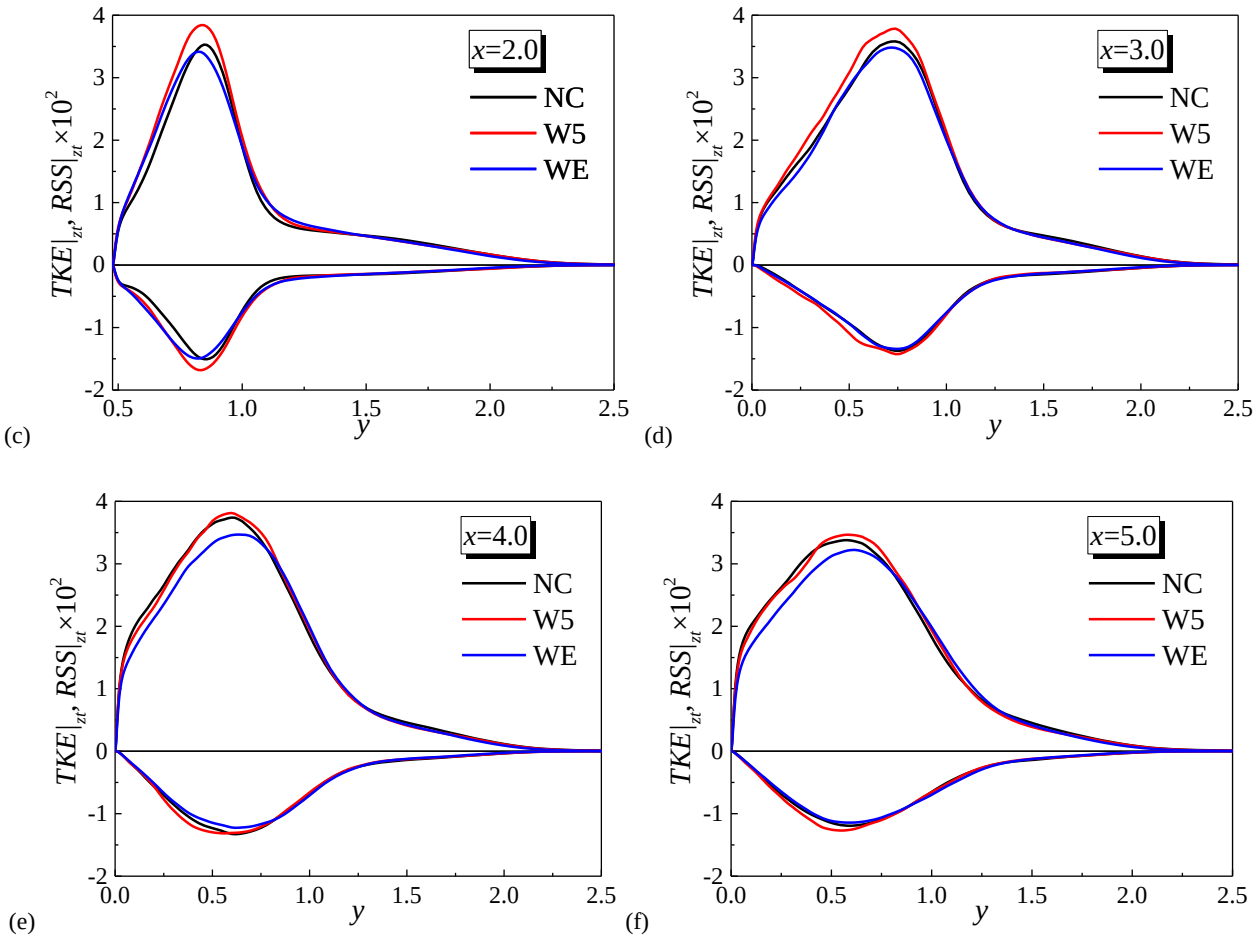


FIG. 13. $TKE|_{zt}$ and $RSS|_{zt}$ calculated by time- and $z$-averaged statistics for Cases NC, W5 and WE at $x$ = 0.0, 0.8, 2.0, 3.0, 4.0 and 5.0, respectively.

The distribution of $TKE|_t$ and $RSS|_t$ based on the time-averaged statistics as well as mean velocity vector $(\bar{w}, \bar{v})$ at six representative streamwise positions for Cases NC, W5 and WE are presented in FIG. 14 and FIG. 15 in order to further study the properties of the LSSVs and the momentum transport. The definition of $TKE|_t$ and $RSS|_t$ is given as,

$$TKE|_t = \frac{1}{2}\overline{u_k' u_k'}/u_{ref}^2 \quad (k = 1,2,3), \tag{13}$$

and

$$RSS|_t = \overline{u'v'}/u_{ref}^2. \tag{14}$$

Both $TKE|_t$ and $RSS|_t$ are normalised by the square of the reference velocity $u_{ref}^2$ in Eqs. (13) and (14). "$|_t$" expresses that the fluctuation is calculated by subtracting the time-averaged velocity from the instantaneous one. It can be seen from FIG. 15 (a)-(c) that, compared with Case NC, the $RSS|_t$ of Cases W5 and WE are reorganised by the alternately distributed OPC and IPC strips. The $RSS|_t$ is enhanced above the IPC strips and the penetration depth is comparable to the local boundary-layer thickness

and thus a spanwise inhomogeneity of the Reynolds shear stress is induced. It can be seen from FIG. 14 (b) and (c) that more turbulent energy is produced in the near-wall regions over the IPC strips following the spanwise variation of $RSS|_t$. Fukagata *et al.* [64] suggested that the Reynolds stress within 80 wall units from the wall is responsible for 90% of the turbulent contribution to the total skin friction drag in a fully developed turbulent pipe flow. Choi *et al.* [51] utilised this to impose OPC into a pipe flow to suppress the near-wall Reynolds stress, resulting in considerable drag reduction. Therefore, the enhanced TKE and RSS above the IPC strips make major contributions to the total skin friction, which is consistent with the variation of $C_f(z)\big|_{x=0.0}$ shown in FIG. 9. A similar distribution of $TKE|_t$ and $RSS|_t$ for the controlled cases can be observed around the separation location, as illustrated in the second rows of FIG. 14 and FIG. 15. As the near-wall turbulence is enhanced downstream of IPC strips, the separation locations of Cases W5 and WE are delayed due to their ability to resist flow separation improved. The control effect with regards to the separation delay is proportional to the width of the IPC strips upstream. This is consistent with the mean separation locations of all the cases summarised in TABLE III. It can be seen from FIG. 14 and FIG. 15 (g) that most of TKE is confined in the free shear-layer for the baseline case after the flow reaches the separated region. However, for Cases W5 and WE, the $TKE|_t$ and $RSS|_t$ in the free shear-layer are redistributed by the sweep and ejection motions. The sweep motions can be observed downstream of IPC as illustrated in FIG. 14 and FIG. 15 (h) and (i). They bring the high momentum fluid from the free shear-layer into the separation bubble, leading to the high $TKE|_t$ and $RSS|_t$ obtained in the near-wall region. The enhanced turbulent momentum transport results in the decrease of the height of the separation bubble as shown by the solid black lines in FIG. 14 and FIG. 15 (h) and (i). It is worth mentioning that the reduction in the height of the separated region is not limited to the regions downstream of the strips, especially for Case W5. It indicates that Case W5 exhibits a better control effect with a narrower width of upstream IPC strips. On the other hand, the ejection motions take the low momentum fluid from the inner part to the outer region of the separation bubble, enhancing the mixing procedure between the recirculation region and the free shear-layer. Compared with Case WE, the $TKE|_t$ and $RSS|_t$ in the free shear-layer downstream of OPC strips are enhanced by Case W5. In the further downstream region, a similar spanwise redistribution of the $TKE|_t$ and $RSS|_t$ in the controlled cases can be observed throughout the whole separation regions, as illustrated in the fourth to fifth rows of FIG. 14 and FIG. 15. As reported by Le *et al.* [65], there exists an oscillatory large-scale roll-up of the shear-layer extending to the reattachment region in the turbulent flow over a backward-facing step, leading to the motion of the reattachment location(s) in the streamwise direction. Therefore, the large-scale structures generated by SADS control interact with the large-scale vortices in the free shear-layer, leading to the reattachment locations being shifted upstream. Since the large-scale motions generated by Case W5 have a relatively stronger impact on the distribution of $TKE|_t$ and $RSS|_t$ in the free shear-layer, the best control effect with regards to the reattachment location is achieved by Case W5. The counter-rotating LSSVs can be clearly seen in the

reattachment regions, as observed in FIG. 14 and FIG. 15 (q) and (r). The spanwise distribution of alternating high-low $TKE|_t$ and $RSS|_t$ streaks corresponds to the low-high mean streamwise velocity streaks in FIG. 10 (q) and (r), exhibiting that the ejection and sweep motions are the major events related to the momentum transports. The penetration depth of the large-scale motions displays the same order of magnitude as the local turbulent boundary-layer thickness.

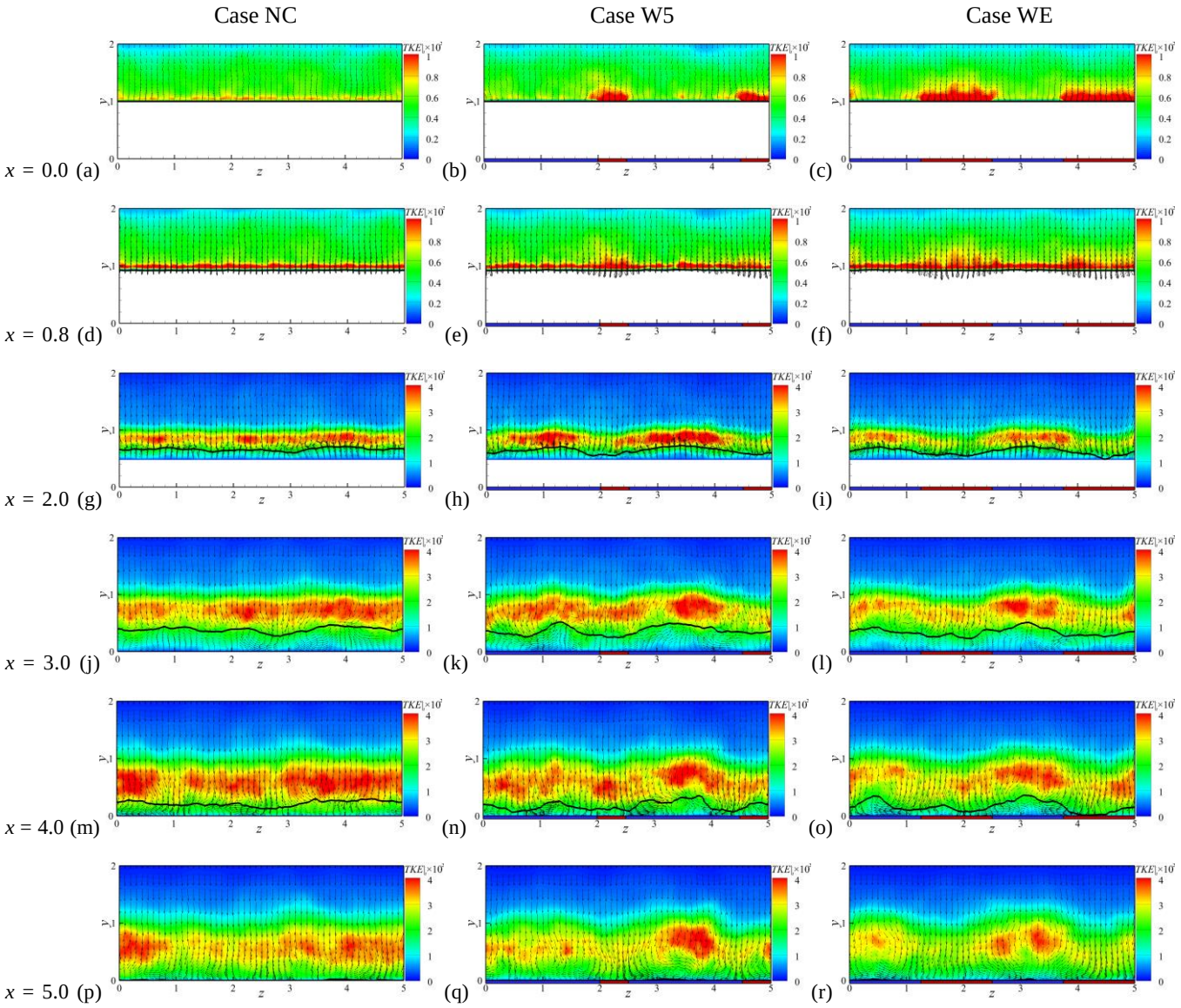


FIG. 14. $TKE|_t$ as well as mean velocity vector $(\overline{w}, \overline{v})$ of Cases NC, W5 and WE from the left-hand-side to the right-hand-side respectively, calculated by time-averaged statistics. The results come from $x$ = 0.0, 0.8, 2.0, 3.0, 4.0, 5.0 from top to bottom. The zero-streamwise-velocity locations are shown as solid black lines for Cases NC, W5 and WE.

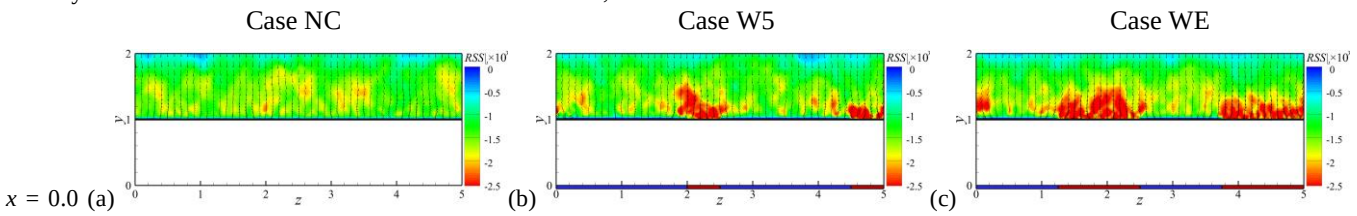

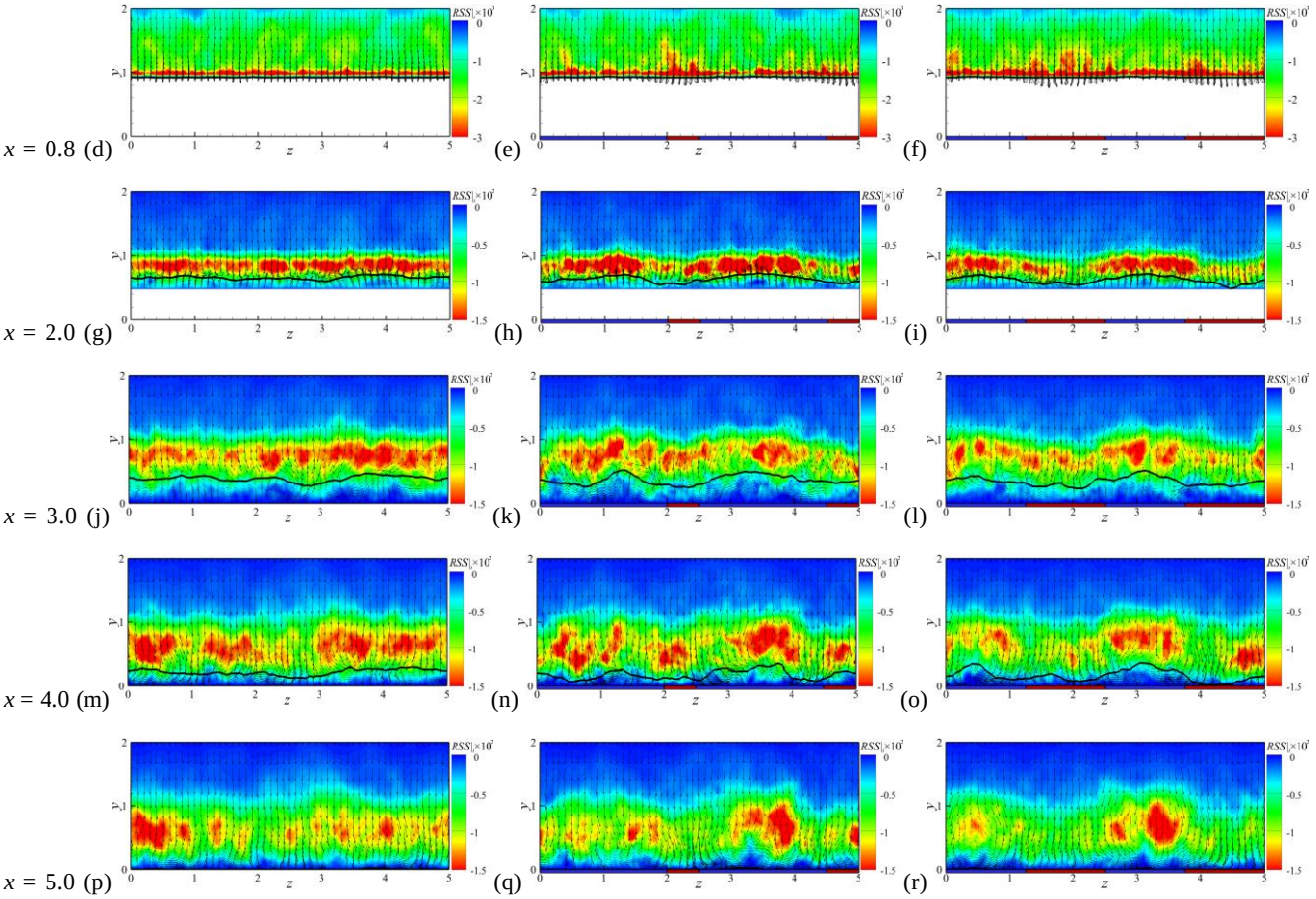


FIG. 15. $RSS|_t$ as well as mean velocity vector $(\bar{w}, \bar{v})$ of Cases NC, W5 and WE from the left-hand-side to the right-hand-side respectively, calculated by time-averaged statistics. The results come from $x$ = 0.0, 0.8, 2.0, 3.0, 4.0 and 5.0 from top to bottom.

To highlight the variation of Reynolds stress in the spanwise direction, two other quantities, namely $\langle\left(u'_{i,\langle z\rangle} - u'_i\right)^2\rangle_z$ and $\langle\left(u'_{\langle z\rangle} - u'\right)\left(v'_{\langle z\rangle} - v'\right)\rangle_z$, are defined in Eqs. (15) and (16) to emphasize the influence of Cases W5 and WE on the modification of the flow field in the spanwise direction,

$$\langle\left(u'_{i,\langle z\rangle} - u'_i\right)^2\rangle_z = \langle(\bar{u}_\iota - \langle\bar{u}_\iota\rangle_z)^2\rangle_z, \tag{15}$$

and

$$\langle\left(u'_{\langle z\rangle} - u'\right)\left(v'_{\langle z\rangle} - v'\right)\rangle_z = \langle(\bar{u} - \langle\bar{u}\rangle_z)(\bar{v} - \langle\bar{v}\rangle_z)\rangle_z. \tag{16}$$

The fluctuations are calculated by subtracting the $z$- and time-averaged velocity from the time-averaged one and $i$ = 1,2,3 in Eqs. (15) and (16). They are normalised by the square of the reference velocity $u_{ref}^2$ as shown in the left-hand-side of FIG. 16 and $\langle\overline{u'^2_{\iota,\langle z\rangle}}\rangle_z$ ($i$ =1,2,3) and $\langle\overline{u'_{\langle z\rangle}v'_{\langle z\rangle}}\rangle_z$ (absolute value), respectively, as illustrated in the right-hand-side of FIG. 16. The results come from $x$ = 0.0, 0.8, 2.0, 3.0, 4.0 and 5.0. It can be seen from FIG. 16 (a) that, compared with Case NC, a doublet structure of the streamwise normal stress is generated at $x$ = 0.0 for Cases W5 and WE. The doublet positions locate at 0.011$H$ ($y^+$ = 5) and 0.086$H$ ($y^+$ = 40) from the wall respectively for Case WE whereas almost the same inner peak position is obtained by Case

W5 and its outer peak is situated slightly away from the wall (0.092$H$, $y^+$ = 35) in comparison with Case WE. As the new definition of the Reynolds stress can exhibit the contribution of spanwise motions to the turbulent intensity by subtracting $\langle\bar{u}\rangle_z$ from $\bar{u}$, we can infer that the doublet value of TKE is induced by the spanwise sharp inhomogeneous variation via alternately distributed strips control in the spanwise direction. The inner peaks for the controlled cases are directly induced by the control method itself. Further, the outer peak position is far away from the wall, indicating the existence of the large-scale motions which should be the LSSVs generated in the logarithmic region of the turbulent boundary layer for the controlled cases. It is worth mentioning that although the turbulent intensity around the inner peak in Case W5 is lower than that in Case WE, a higher outer peak value is obtained in the former case. We assume that more intense large-scale structures are generated by Case W5 and then interact with the downstream free shear-layer leading to a better performance with regards to the reattachment point shifting upstream, as shown in TABLE III. The momentum transport of Cases W5 and WE are enhanced in the near-wall region, leading to a significant rise of the streamwise component of turbulent intensity with a same peak position (inner peak) compared to the Reynolds shear stress. The other two normal Reynolds stresses increase as well in comparison with those of Case NC, as shown in FIG. 16 (a). Another normalisation using the local $\langle\overline{u'^2_{i,\langle z\rangle}}\rangle_z$ ($i$ =1,2,3) and $\langle\overline{u'_{\langle z\rangle}v'_{\langle z\rangle}}\rangle_z$ is presented in FIG. 16 (b). A doublet structure of the streamwise normal stress can also be observed. However, both the inner and outer peak values of Case W5 are higher than those of Case WE, showing that Case W5 induces a relatively stronger spanwise inhomogeneity with regards to the local Reynolds stresses in comparison with Case WE. Thus, it can be concluded that the large-scale structures are generated by SADS control, and they play a significant role in the production of Reynolds stresses. Case W5 is more efficient in creating large-scale structures, although Case WE produces more turbulent energy locally in the near-wall region due to its wider IPC strips. Further, it can be seen from the left-hand-side of FIG. 16 that the large-scale spanwise inhomogeneity induced by SADS control can be sustained in the downstream of separated region, even extending to the flow recovery region (FIG. 16 (k)). The streamwise Reynolds normal stress and Reynolds shear stress in the controlled cases are enhanced in comparison with Case NC. The near-wall peak of the streamwise Reynolds normal stress disappears over the rounded ramp and the downstream reattachment region since the OPC and IPC strips are only imposed onto the flat plate surface upstream of the rounded ramp. However, the outer peaks are maintained in the downstream region and situated around the core of the free shear-layer. This indicates that the large-scale structures generated by SADS control can be sustained in the downstream area and interact with the free shear-layer, leading to momentum transport enhancement and the reattachment points being shifted upstream.

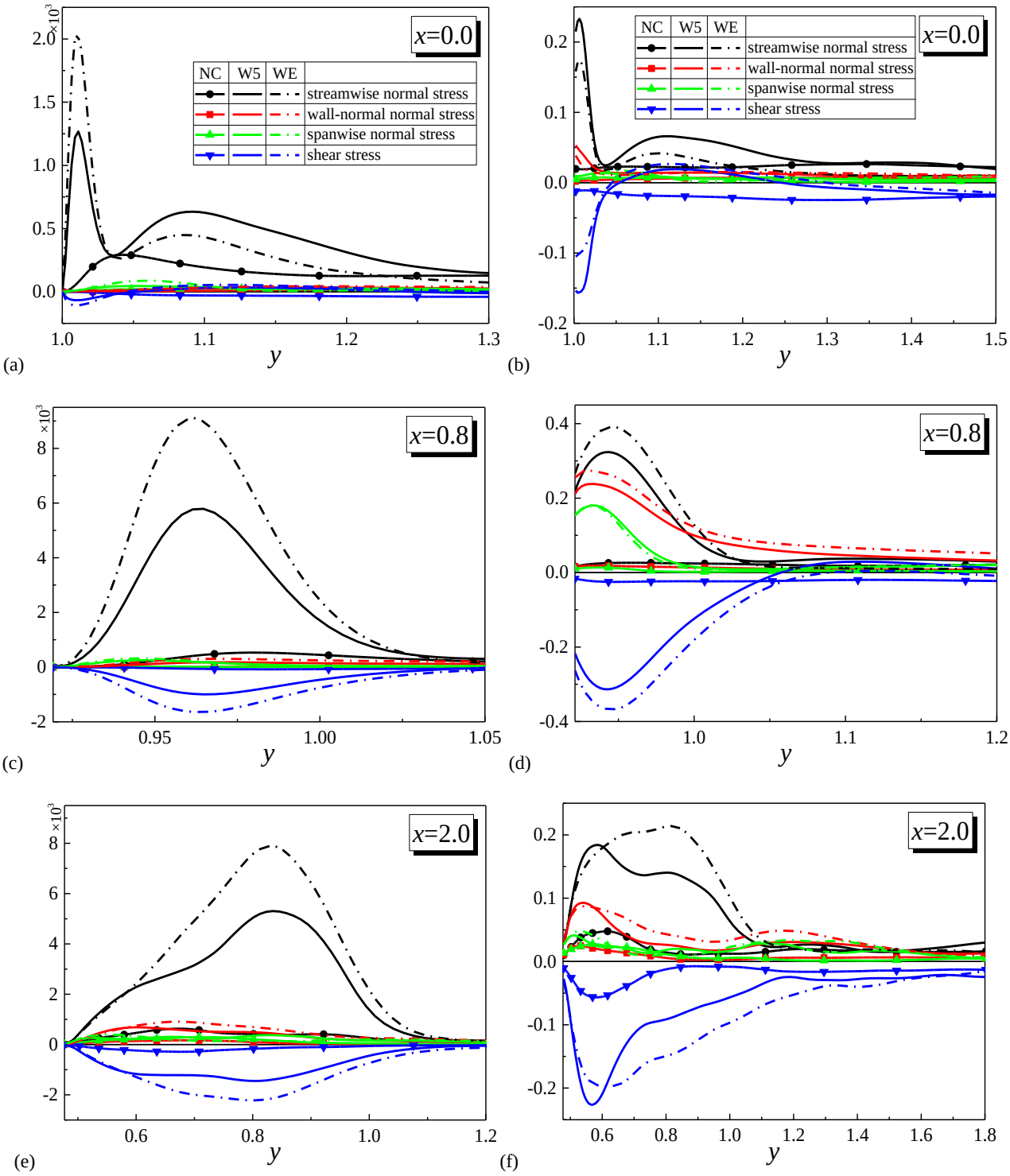
x=0.0
NC
W5
WE
streamwise normal stress
wall-normal normal stress
spanwise normal stress
shear stress
×10^3
y
(a)
(b)
x=0.8
(c)
(d)
x=2.0
(e)
(f)

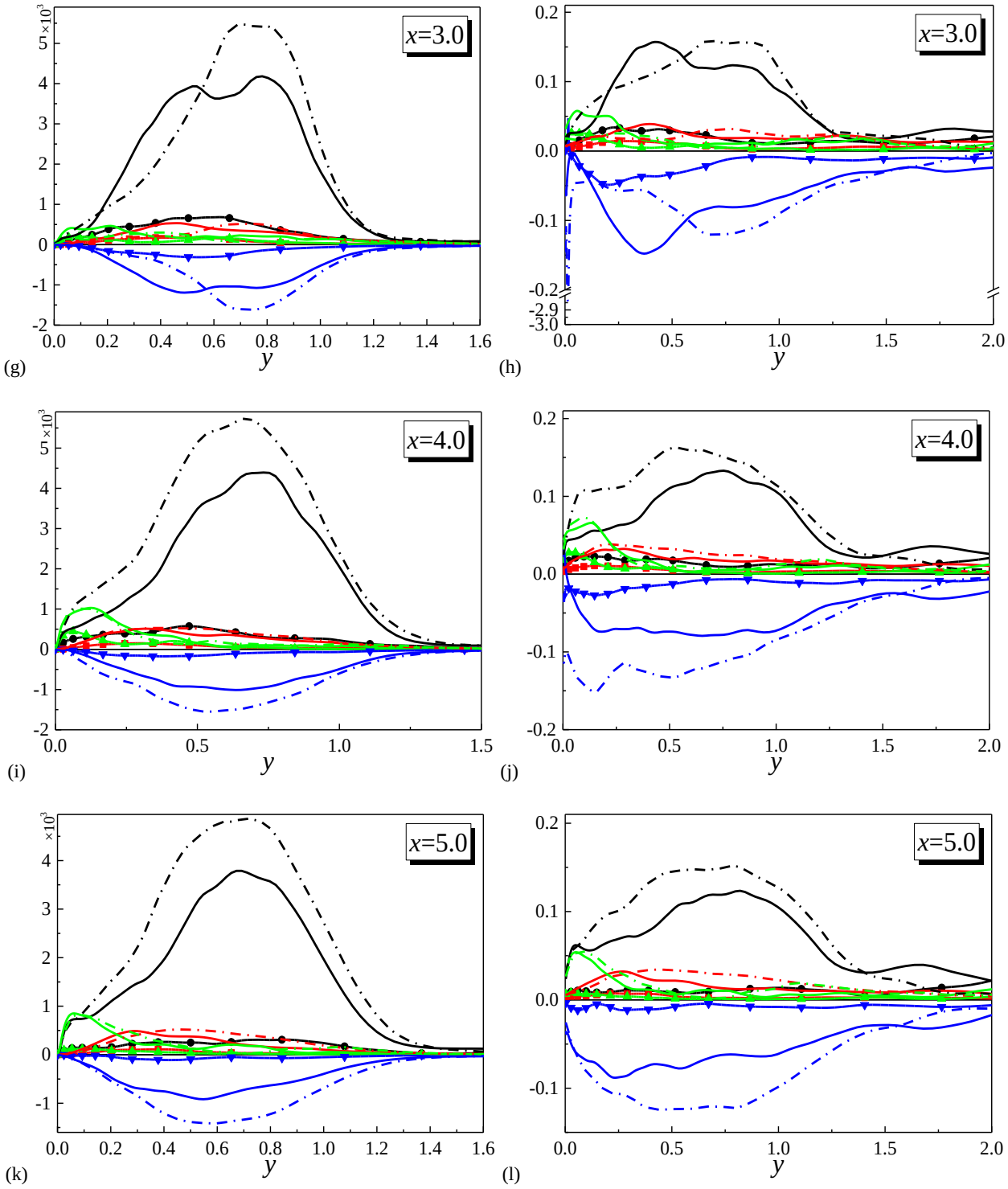


FIG. 16. Turbulent intensity $\langle\left(u'_{i,\langle z\rangle}-u'_i\right)^2\rangle_z$ and Reynolds shear stress $\langle\left(u'_{\langle z\rangle}-u'\right)\left(v'_{\langle z\rangle}-v'\right)\rangle_z$ of Cases NC (line with symbols), W5 (solid lines) and WE (dash-dot lines) normalised by the square of the reference velocity $u^2_{ref}$ (left-hand-side) and $\langle\overline{u'^2_{i,\langle z\rangle}}\rangle_z$ ($i$ =1,2,3) and $\langle\overline{u'_{\langle z\rangle}v'_{\langle z\rangle}}\rangle_z$ (absolute value) respectively (right-hand-side). The definition of $\langle\left(u'_{i,\langle z\rangle}-u'_i\right)^2\rangle_z$ and $\langle\left(u'_{\langle z\rangle}-u'\right)\left(v'_{\langle z\rangle}-v'\right)\rangle_z$ refer to Eqs. (15) and (16). The results come from $x$ = 0.0, 0.8, 2.0, 3.0, 4.0 and 5.0 from top to bottom.

## IV. CONLUSIONS and PERSPECTIVE

The $M$ = 0.2 turbulent boundary-layer flow separation from a backward-facing rounded ramp with spanwise alternating distributed strips control is investigated using implicit large-eddy simulation. Flow control is achieved by imposing spanwise alternating distributed out-of-phase control and in-phase control of wall velocity actuations onto a fully developed turbulent boundary layer upstream of the rounded ramp. The generation of large-scale streamwise vortices by such a small-scale control device and their interaction with the downstream separated region are focused on. The following conclusions are reached:

- With spanwise alternating distributed out-of-phase/in-phase control strips, the distribution of the flow field can be modified in the spanwise direction. Turbulence coherent structures are alternatively suppressed and enhanced over out-of-phase and in-phase control regions for all controlled cases. The mean velocity located in the controlled regions are reorganised along the spanwise direction and vertical shear-layers are created between neighbouring out-of-phase and in-phase control strips.

- The analyses confirm that the large-scale streamwise vortices are generated by spanwise alternating distributed strips control. They have an effective interaction with the downstream free shear-layer and reduce the size of the separation bubble. The large-scale structures induced by the control method enhance momentum transport in the spanwise direction. The sweep motion goes towards the wall downstream of the in-phase control strip, bringing the high TKE and RSS from the free shear-layer into the reverse flow zone, leading to the size of the recirculation region being reduced, and the ejection motion moves away from the wall downstream of the out-of-phase strip and an increase in the size of the separation bubble is induced. Consequently, the flow in the separated region presents a strong 3-D characteristic, and the overall reduction of the mean separation zone is achieved due to the delay of the separation and the upstream shift of the reattachment.

- The delay of the separation point is attributed to the local activation of the near-wall turbulence by in-phase control and the performance improvement with regards to the reattachment location shifting upstream is mainly due to the presence of the large-scale streamwise vortices.

- The turbulence intensity above the regions downstream of the in-phase control strips is enhanced and thus the flow has a stronger ability to resist the flow separation. Therefore, the best performance with regards to the separation point is achieved by Case WE. However, Case W5 is considered as the best in terms of the reattachment point and the length of the separation zone It shows that there exists another control mechanism, *i.e.* the interactions between the large-scale streamwise vortices and flow separation, which dominates the reattachment. Besides, a much lower skin friction is induced by Case W5 on the control surface due to its narrower in-phase control strips. Therefore, it is regarded as the optimal case in terms of the overall performance among all the cases studied.

The effect of the Reynolds number and the Mach number on the flow separation control is outside the scope of this study and will be attempted in future.

## ACKNOWLEDGMENTS

The project is supported by Department of Research and Advanced Engineering of PSA, the UK Turbulence Consortium (EP/L000261/1) and the UK Consortium of Turbulent Reacting Flows (EP/K024574/1) under EPSRC, National Natural Science Foundation of China (51420105008, 11572025 and 51476004), and the National Basic Research Program of China (2014CB046405). Weidan Ni was supported by the China Scholarship Council for one-year study at the Science and Technology Facilities Council Daresbury Laboratory of the United Kingdom. The simulations were conducted on the Academic Research Computing High End Resource (ARCHER) supercomputer. David Emerson gratefully acknowledges additional financial support from EPSRC under grants EP/N016602/1EP/L00030X/1 and EP/K038451/1.

## REFERENCES

[1]M. Gad-el-Hak. "Flow Control: Passive, Active, and Reactive Flow Management," Cambridge University Press, London, pp. 2(2000).

[2]L. Prandtl. "Über Flussigkeitsbewegung bei sehr kleiner Reibung," in Proc. Third Int. Math. Cong., Heidelberg, Germany, 484(1904).

[3]M. Gad-el-Hak and D.M. Bushnell. "Separation control: Review," J. Fluids Eng. 113, 5(1991).

[4]M.A. Leschziner, H. Choi and K.S. Choi. "Flow-control approaches to drag reduction in aerodynamics: progress and prospects," Phil. Trans. R. Soc. A 369, 1349(2011).

[5]H.D. Taylor. "The elimination of diffuser separation by vortex generators," United Aircraft Corporation Report No. R-4012-3(1947).

[6]J.C. Lin. "Review of research on low-profile vortex generators to control boundary-layer separation," Prog. Aerosp. Sci. 38, 389(2002).

[7]K. Koeltzsch, A. Dinkelacker and R. Grundmann. "Flow over convergent and divergent wall riblets. Experiments in Fluids," 33, 346(2002).

[8]B. Nugroho, N. Hutchins and J.P. Monty. "Large-scale spanwise periodicity in a turbulent boundary layer induced by highly ordered and directional surface roughness," Int. J. Heat Fluid Fl. 41, 90(2013).

[9]R. Mejia-Alvarez, J.M. Barros and K.T. Christensen. "Structural attributes of turbulent flow over a complex topography," Coherent Flow Structures at Earth's Surface, 25(2013).

[10]R. Mejia-Alvarez and K.T. Christensen. “Wall-parallel stereo particle-image velocimetry measurements in the roughness sublayer of turbulent flow overlying highly irregular roughness,” Phys. Fluids, 25, 115109(2013).

[11]S.J. Kline, W.C. Reynolds, F.A. Schraub and P.W. Rundstadler. “The structure of turbulent boundary layers,” J. Fluid Mech. 30, 741(1967).

[12]S.K. Robinson. “Coherent motions in the turbulent boundary layer,” Annu. Rev. Fluid Mech. 23, 601(1991).

[13]W. Schoppa and F. Hussain. “Coherent structure generation in near-wall turbulence,” J. Fluid Mech. 453, 57(2002).

[14]B. Ganapathisubramani, E.K. Longmire and I. Marusic. “Characteristics of vortex packets in turbulent boundary layers,” J. Fluid Mech. 478, 35(2003).

[15]C.D. Tomkins and R.J. Adrian. “Spanwise structure and scale growth in turbulent boundary layers,” J. Fluid Mech. 490, 37(2003).

[16]J.M. Barros, and K.T. Christensen. “Observations of turbulent secondary flows in a rough-wall boundary layer.” J. Fluid Mech. 748, R1(2014).

[17]D. Willingham, W. Anderson, K.T. Christensen and J.M. Barros. “Turbulent boundary layer flow over transverse aerodynamic roughness transitions: Induced mixing and flow characterization,” Phys. Fluids 26, 025111(2014).

[18]H.L. Bai, Kevin, N. Hutchins and J.P. Monty. “Turbulence modifications in a turbulent boundary layer over a rough wall with spanwise-alternating roughness strips,” Phys. Fluids, 30, 055105(2018).

[19]K. Kevin, J.P. Monty, H.L. Bai, G. Pathikonda, B. Nugroho, J.M. Barros, K.T. Christensen and N. Hutchins. “Cross-stream stereoscopic particle image velocimetry of a modified turbulent boundary layer over directional surface pattern,” J. Fluid Mech., 813, 412(2017).

[20]J.O. Hinze. “Secondary currents in wall turbulence,” Phys. Fluids 10, S122(1967).

[21]J.O. Hinze. “Experimental investigation on secondary currents in the turbulent flow through a straight conduit,” Appl. Sci. Res. 28, 453(1973).

[22]A. Stroh, Y. Hasegawa, J. Kriegseis and B. Frohnapfel. “Secondary vortices over surfaces with spanwise varying drag,” J. Turbul. 17, 1142(2016).

[23]H.G. Hwang and J.H. Lee. “Secondary flows in turbulent boundary layers over longitudinal surface roughness,” Phys. Rev. Fluids, 3, 014608(2018).

[24]C. Vanderwel and B. Ganapathisubramani. “Effects of spanwise spacing on large-scale secondary flows in rough-wall turbulent boundary layers,” J. Fluid Mech. 774, R2(2015).

[25]J. Yang and W. Anderson. “Numerical study of turbulent channel flow over surfaces with variable spanwise heterogeneities: Topographically-driven secondary flows affect outer-layer similarity of turbulent length scales,” Flow Turbul. Combust. 100, 1(2018).

[26]D. Chung, J.P. Monty and N. Hutchins. “Similarity and structure of wall turbulence with lateral wall shear stress variations,” J. Fluid Mech. 847, 591(2018).

[27]W. Anderson, J.M. Barros, K.T. Christensen and A. Awashi. “Numerical and experimental study of mechanisms responsible for turbulent secondary flows in boundary layer flows over spanwise heterogeneous roughness,” J. Fluid Mech. 768, 316(2015).

[28]A.A. Townsend. “The Structure of Turbulent Shear Flow,” Cambridge University Press, London, pp. 259(1956).

[29]F. Xu, S. Zhong and S. Zhang. “Vortical structures and development of laminar flow over convergent-divergent riblets,” Phys. Fluids, 30, 051901(2018).

[30]R. Mejiaalvarez and K.T. Christensen. “Low-order representations of irregular surface roughness and their impact on a turbulent boundary layer,” Phys. Fluids 22, 015106(2010).

[31]T. Medjnoun, C. Vanderwel and B. Ganapathisubramani. “Characteristics of turbulent boundary layers over smooth surfaces with spanwise heterogeneities,” J. Fluid Mech. 838, 516(2018).

[32]D.A. Vermaas, W.S.J. Uijttewaal and A.J.F. Hoitink. “Lateral transfer of streamwise momentum caused by a roughness transition across a shallow channel,” Water Resources Research 47, 2144(2011).

[33]W. Ni, L. Lu, J. Fang, C. Moulinec and Y. Yao. “Large-scale streamwise vortices in turbulent channel flow induced by active wall actuations,” Flow Turbul. Combust. 100, 651(2018).

[34]W. Ni, L. Lu, J. Fang, C. Moulinec and Y. Yao. “Direct numerical simulation of turbulent channel flow with spanwise alternatively distributed strips control,” Mod. Phys. Lett. B 32, 1840004(2018).

[35]S. Lardeau and M.A. Leschziner. “The interaction of round synthetic jets with a turbulent boundary layer separating from a rounded ramp,” J. Fluid Mech. 683, 172(2011).

[36]Y. Bentaleb, S. Lardeau and M.A. Leschziner. “Large-eddy simulation of turbulent boundary layer separation from a rounded step,” J. Turbul. 13, N4(2012).

[37]N. Hutchins and I. Marusic. “Large-scale influences in near-wall turbulence,” Philos. T. R. Soc. A 365, 1852 (2007).

[38]J. Fang, Y. Yao, Z. Li and L. Lu. “Investigation of low-dissipation monotonicity-preserving scheme for direct numerical simulation of compressible turbulent flows,” Comput. Fluids 104, 55(2014).

[39]J. Fang, Y. Yao, A.A. Zheltovodov, Z. Li and L. Lu. “Direct numerical simulation of supersonic turbulent flows around a tandem expansion-compression corner,” Phys. Fluids 27, 125104 (2015).

[40]J. Fang, Y. Yao, A.A. Zheltovodov and L. Lu. “Investigation of three-dimensional shock wave/turbulent boundary layer interaction initiated by a single fin,” AIAA J. 55, 509(2016).

[41]S.K. Lele. “Compact finite difference schemes with spectral-like resolution,” J. Comput. Phys. 103, 16(1992).

[42]N.D. Sandham, Q. Li and H.C. Yee. “Entropy splitting for high–order numerical simulation of compressible turbulence,” J. Comput. Phys. 178, 307(2002).

[43]D.V. Gaitonde and M.R. Visbal. “Pade-Type Higher-Order Boundary Filters for the Navier–Stokes Equations,” AIAA Paper No. 2103-2112(2000).

[44]L. Fang, W.J. Bos, L. Shao, and J.P. Bertoglio. “Time-reversibility of Naver-Stokes turbulence and its implication for subgrid scale models,” J. Turb. 13, 1(2012).

[45]L. Fang, L. Shao, and P. Bertoglio. “Recent understanding on the subgrid-scale modeling of large-eddy simulation in physical space,” Sci. China Phys. Mech. 57, 2188(2014).

[46]M.R. Visbal and D.P. Rizzetta. “Large-Eddy Simulation on Curvilinear Grids Using Compact Differencing and Filtering Schemes,” J. Fluid Eng. 124, 836(2002).

[47]D.P. Rizzetta, M.R. Visbal and G.A. Blaisdell. “A time-implicit high-order compact differencing and filtering scheme for large-eddy simulation,” Int. J. Numer. Meth. Fluids 42, 665(2003).

[48]M.R. Visbal, P.E. Morgan, and D.P. Rizzetta. “An Implicit LES Approach Based on High-Order Compact Differencing and Filtering Schemes,” AIAA Paper No. 2003-4098(2003).

[49]D.P. Rizzetta, M.R. Visbal and P.E. Morgan. “A High-Order Compact Finite-Difference Scheme for Large-Eddy Simulation of Active Flow Control,” AIAA Paper No. 2008-526(2008).

[50]S. Gottlieb, and C.W. Shu. “Total variation diminishing Runge–Kutta schemes,” Math. Comput. 67, 73(1998).

[51]H. Choi, P. Moin and J. Kim. “Active turbulence control for drag reduction in wall-bounded flows,” J. Fluid Mech. 262, 75(1994).

[52]J.W. Kim and D.J. Lee, “Generalized characteristic boundary conditions for computational aeroacoustics,” AIAA J. 38, 2040(2000).

[53]J.W. Kim and D.J. Lee, “Generalized characteristic boundary conditions for computational aeroacoustics, part 2,” AIAA J. 41, 47(2004).

[54]E. Touber and N.D. Sandham. “Large-eddy simulation of low-frequency unsteadiness in a turbulent shock-induced separation bubble,” Theor. Comput. Fluid Dyn., 23, 79(2009).

[55]B. Morgan, J. Larsson, S. Kawai and S.K. Lele. “Improving low-frequency characteristics of recycling/rescaling inflow turbulence generation,” AIAA J., 49, 582(2011).

[56]J.W. Kim and D.J. Lee. “Generalized characteristic boundary conditions for computational aeroacoustics,” AIAA J. 38, 2040(2000).

[57]J.W. Kim and D.J. Lee. “Generalized characteristic boundary conditions for computational aeroacoustics, part 2,” AIAA J. 41, 47(2004).

[58]P. Schlatter and R. Örlü. “Assessment of direct numerical simulation data of turbulent boundary layers,” J. Fluid Mech. 659, 116(2010).

[59]J. Fang, Y. Yao, A.A. Zheltovodov, Z. Li, and L. Lu. “Direct numerical simulation of supersonic turbulent flows around a tandem expansion-compression corner,” Phys. Fluids, 27, 125104(2015).

[60]J. Jiménez, S. Hoyas, M.P. Simens and Y. Mizuno. “Turbulent boundary layers and channels at moderate Reynolds numbers,” J. Fluid Mech. 657, 335(2010).

[61]L. Duan, I. Beekman and M.P. Martin. “Direct numerical simulation of hypersonic turbulent boundary layers. Part 2. Effect of wall temperature,” J. Fluid Mech. 655, 419 (2010).

[62]J.C.R. Hunt, A.A. Wray and P. Moin. “Eddies, streams, and convergence zones in turbulent flows,” Center for Turbulence Research Report CTR-S88, p. 193(1988).

[63]R. Legendre. “Lignes de courant en écoulement permanent: Décollement et séparation (Streamlines in permanent flows: Detachment and separation),” La Recherche Aérospatiale, No. 1977–6(1977).

[64]K. Fukagata, K. Iwamoto and N. Kasagi. “Contribution of Reynolds stress distribution to the skin friction in wall-bounded flows,” Phys. Fluids, 14, L73(2002).

[65]H. Le, P. Moin and J. Kim. “Direct numerical simulation of turbulent flow over a backward-facing step,” J. Fluid Mech., 330, 349 (1997).

## APPENDIX

The mesh resolution normalised by local Kolmogorov length scale for the baseline case is checked a posteriori as shown in Figure A, where $\Delta = \sqrt[3]{\Delta x \Delta y \Delta z}$ is the effective mesh spacing and $\Delta x$, $\Delta y$ and $\Delta z$ refer to the local grid spacing in the streamwise, wall-normal and spanwise direction, respectively. The Kolmogorov scale is calculated by $\eta = \left(\frac{\langle \bar{\mu} \rangle_z}{\langle \bar{\rho} \rangle_z \langle \bar{\varepsilon} \rangle_z}\right)^{1/4}$, where $\varepsilon$ is the dissipation term of the turbulence kinetic energy (TKE) equation. The ratio of the effective mesh spacing to the local Kolmogorov length scale calculated with the solved dissipation $\langle \bar{\varepsilon} \rangle_z$ is less than 3.8 throughout the computational zone. However, a further analysis of the TKE budgets (seen in Figure B) shows that the maximum ratio of the numerical residual to the resolved TKE dissipation is up to 70% in the separation zone. Therefore, the simulations in this paper are regarded as ILES.

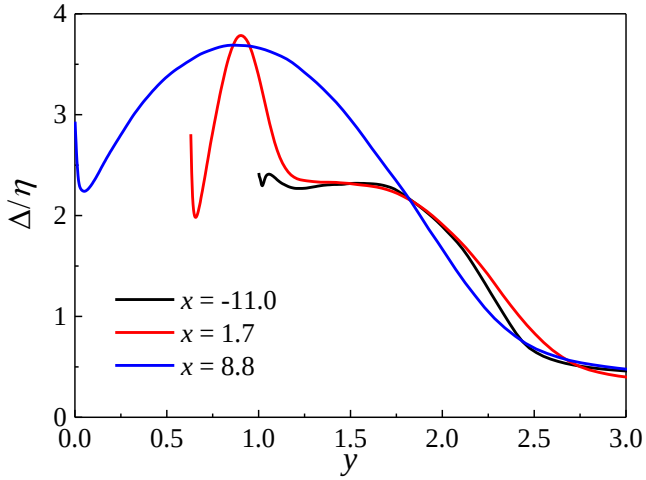


Figure A. Mesh resolution at three representative streamwise locations for the baseline case. Δ is the mesh scale and $\eta$ is the Kolmogorov scale based on the resolved dissipation.

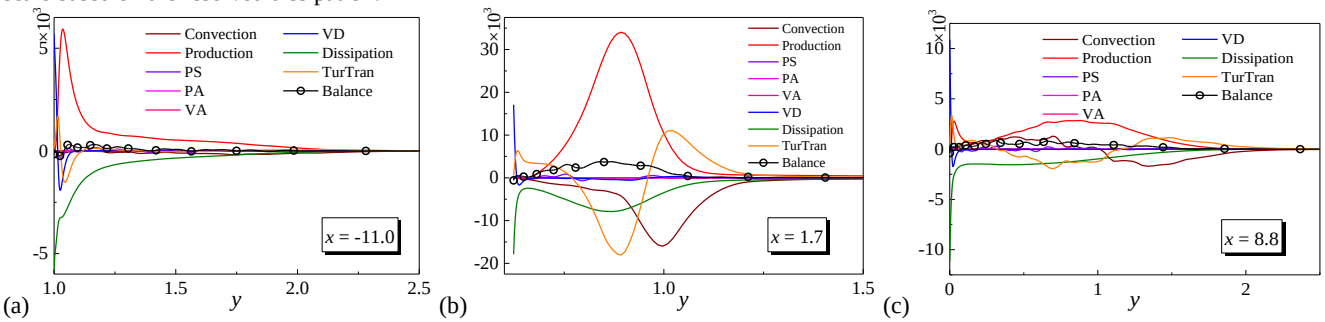


Figure B. TKE budgets at three representative streamwise locations for the baseline case.